bioRxiv preprint doi: https://doi.org/10.1101/2021.09.13.460097; this version posted April 19, 2022. The copyright holder for this preprint (which was not certified by peer review) is the author/funder. All rights reserved. No reuse allowed without permission.

Orientation dependent proton transverse relaxation in the human brain white matter: The magic angle effect on a cylindrical helix

Yuxi Pang, PhD

Department of Radiology, University of Michigan, Ann Arbor, MI, USA

Corresponding Author:

Yuxi Pang, PhD
University of Michigan Hospital
1500 E. Medical Center Dr., UH B2 RM A205F
Ann Arbor, MI 48109-5030, USA
Tel: 734-232-6585
Fax: 734-764-2412
Email: yuxipang@umich.edu
Twitter: @yuxipang
ORCID iD: Yuxi Pang (https://orcid.org/0000-0001-5039-0236)

Running Title: Orientation dependent proton transverse relaxation in white matter

Word Count: 5911

bioRxiv preprint doi: https://doi.org/10.1101/2021.09.13.460097; this version posted April 19, 2022. The copyright holder for this preprint (which was not certified by peer review) is the author/funder. All rights reserved. No reuse allowed without permission.

ABSTRACT

Purpose: To overcome some limitations of prior orientation-dependent proton transverse relaxation formalisms in white matter (WM) with a novel framework based on the generalized magic angle effect function.

Methods: A cylindrical helix model was developed embracing anisotropic rotational and translational diffusion of restricted molecules in human brain WM, with the former characterized by an axially symmetric system. Transverse relaxation rates R_2 and R_2^* were divided into isotropic R_2^i and anisotropic parts, $R_2^a * f(\alpha, \Phi - \varepsilon_0)$, with α denoting an open angle and ε_0 an orientation (Φ) offset from DTI-derived primary diffusivity direction. The proposed framework (Fit A) was compared with prior models without ε_0 on previously published water and methylene proton transverse relaxation rates from developing, healthy, and pathological WM at 3T. Goodness of fit was represented by root-mean-square error (RMSE). F-test and linear correlation were used with statistical significance set to $P \leq 0.05$.

Results: Fit A significantly (P<0.01) outperformed prior models as demonstrated by reduced RMSEs, e.g., 0.349 vs. 0.724 in myelin water. Fitted ε_0 was in good agreement with calculated ε_0 from directional diffusivities. Compared with those from healthy adult, the fitted R_2^i, R_2^a, and α from neonates were substantially reduced but ε_0 increased, consistent with incomplete myelination. Significant positive (R_2^i) and negative (α and R_2^a) correlations were found with aging (demyelination) in elderly.

Conclusion: The developed framework can better characterize orientation dependences from a wide range of proton transverse relaxation measurements in human brain WM, shedding new light on myelin microstructural alterations at the molecular level.

Keywords: cylindrical helix model, diffusion tensor imaging, quantitative magnetization transfer, magic angle effect, orientation-dependent transverse relaxation**,** principal diffusivity direction, white matter.

Abbreviations: AR, angular resolution; CPMG, Carr-Purcell-Meiboom-Gill; CNT, control; DTI, diffusion tensor imaging; FA, fractional anisotropy; IE, intra- and extra-cellular; MAE, magic angle effect; MO, mode of anisotropy; MS, multiple sclerosis; PCC, Pearson correlation

bioRxiv preprint doi: https://doi.org/10.1101/2021.09.13.460097; this version posted April 19, 2022. The copyright holder for this preprint (which was not certified by peer review) is the author/funder. All rights reserved. No reuse allowed without permission.

coefficient; qMT, quantitative magnetization transfer; RDC, residual dipolar coupling; RMSE, root-mean-square error; SBL, siblings; WM, white matter

1 | INTRODUCTION

The intrinsic contrast of MR imaging of biological tissues comes mostly from spatial variations in proton relaxation rates,[1] which are reflective of local environments and governed by varying molecular motions on different timescales.[2, 3] In principle, proton relaxation measurements can provide basic microstructural information particularly for tissues with highly organized microarchitectures. For instance, myelinated axons in the human brain white matter (WM) are anisotropic and inhomogeneous in nature and water proton longitudinal (i.e., R_1=$1/T_1$) and transverse (i.e., R_2=$1/T_2$) relaxation rates have been revealed depending on orientations of axon fibers although the reported R_1 relaxation anisotropy at 3T is much smaller than that of R_2.[4-7]

Based on water proton transverse magnetization dephasing induced by applied directional diffusion gradients, diffusion tensor imaging (DTI) can provide axon orientation information in WM at an image voxel size level.[8, 9] Generally, three orthogonal translational diffusivities (i.e., eigenvalues) and the corresponding directions (i.e., eigenvectors) relative to an external static magnetic field B_0 can be determined based on the standard DTI model. While the magnitude of anisotropic diffusion can be well defined from the diffusion tensor eigenvalues, it remains unclear whether the direction of anisotropic diffusion can accurately represent an axon fiber direction, which is usually assumed as the direction of principal diffusivity.[9, 10] When the direction of principal diffusivity was used as an internal orientation gold standard, some discrepancies appeared when compared with an axon orientation derived from either susceptibility tensor imaging[11-14] or nanostructure-specific X-ray tomography.[15] Similarly, when this internal reference was used to guide the orientation dependence of proton transverse (R_2 and

bioRxiv preprint doi: https://doi.org/10.1101/2021.09.13.460097; this version posted April 19, 2022. The copyright holder for this preprint (which was not certified by peer review) is the author/funder. All rights reserved. No reuse allowed without permission.

R_2^*) relaxation in vivo, the observed orientation dependence profiles manifested an angle offset ε_0 that has not yet been accounted for.[4, 16-18] Herein, R_2 and R_2^* were treated equally regarding the axon fiber orientation dependences on B_0.

In the past, susceptibility-based relaxation models have been proposed for characterizing anisotropic R_2 and R_2^* in WM,[14, 19-21] expressed either by $A_1 + A_2 \cos 2\theta + A_3 \cos 4\theta$ or by $B_1 + B_2 \sin^2\theta + B_3 \sin^4\theta$. Here, θ is the angle between an axon fiber and B_0, A_i and B_i $(i = 1,2,3)$ the model parameters (i.e., trigonometric function coefficients). As revealed recently,[7, 18] both functions are mathematically equivalent albeit with different coefficients. More importantly, these coefficients are not mutually independent as $\cos 4\theta$ (or $\sin^4\theta$) can be expressed by $\cos 2\theta$ (or $\sin^2\theta$) and vice versa; thus, any proposed biophysical interpretations of fitted model parameters will become ambiguous.

When considered as the potential origin of anisotropic R_2 and R_2^* in WM, the magic angle effect (MAE) had not been appropriately evaluated in the literature.[20, 22] Typically, the standard MAE function (i.e., orientation dependence) is written as $(3\cos^2\theta - 1)^2$, indicating that MAE will disappear with θ=54.7° (i.e., "magic angle") and will be four times less with θ=90° than that with θ=0°. However, the observed R_2 and R_2^* in WM contradicted this theoretical predication; in other words, the reported R_2 and R_2^* became larger when θ changed from 0° to 90°. As a result, MAE had been ruled out as a potential relaxation mechanism. It should be emphasized that this standard MAE function implicitly assumes that all restricted water molecules are uniformly orientated along the same direction, which might not be the case in brain WM.[23] A general form of MAE function has long been available[24] and lately reformatted to gain further insight into proton transverse relaxation orientation dependences.[25]

bioRxiv preprint doi: https://doi.org/10.1101/2021.09.13.460097; this version posted April 19, 2022. The copyright holder for this preprint (which was not certified by peer review) is the author/funder. All rights reserved. No reuse allowed without permission.

As both stemmed from thermally driven Brownian motions, molecular translational diffusion and rotational diffusion (or reorientation) should be intimately linked,[7, 26, 27] with the former probed by DTI and the latter by MR relaxation measurements. To our knowledge, no direct connection exists between the two different measurements for studying the same anisotropic microstructures in WM.[28] This disconnection might impede better characterization of rotationally restricted molecules both on the surface (water, H2O) and in the interior (lipid methylene, CH2)[29, 30] of phospholipid bilayers in WM. In the past, an ultrashort transverse relaxation time (T_2^b~10-15 μs) of semisolid lipid CH2 protons was observed by quantitative magnetization transfer (qMT) imaging,[31] revealing the comparable orientation dependence with respect to that of surface water based on multiple orientation-dependent transverse relaxation studies in literature.[4, 7, 17, 18, 32]

The aim of this work was thus to introduce an angle offset ε_0, determined by DTI diffusivities, into a cylindrical helix model based on the generalized MAE function for characterizing anisotropic transverse relaxation of ordered water and semisolid CH2 protons in WM. The proposed theoretical framework was validated by a high-resolution Connectome DTI dataset and then applied to previously published anisotropic R_2 and R_2^* profiles at 3T in vivo from the human brain WM of neonates, healthy and diseased adults. The results demonstrate that the proposed model can better characterize the documented orientation-dependent proton transverse relaxation profiles.

2 | THEORY

Water molecular reorientation in biological tissues, unlike in solution, becomes restricted to some extent,[33] giving rise to a non-averaged dipolar interaction between two intramolecular

bioRxiv preprint doi: https://doi.org/10.1101/2021.09.13.460097; this version posted April 19, 2022. The copyright holder for this preprint (which was not certified by peer review) is the author/funder. All rights reserved. No reuse allowed without permission.

proton nuclei, referred to herein as residual dipolar coupling (RDC) and signified by <H-H>. If the water rapidly rotates preferentially around a cylindrically symmetric axis that makes an angle β with <H-H> and an angle θ with B_0, this RDC can be expressed by $DD * P_2(\cos\beta)P_2(\cos\theta)$,[34, 35] with the constant DD denoting the theoretical dipolar interaction strength for a rigidly fixed water and $P_2(x) = (3x^2 - 1)/2$ the second order Legendre polynomial. $P_2(\cos\theta)$ indicates the orientation dependence of RDC and $P_2(\cos\beta)$ is called "order parameter" in literature.[35, 36] It has long been known[24] that water proton signal splitting in partially hydrated tissues is proportional to the mean of RDC, i.e., $\langle P_2(\cos\theta)\rangle$, and the corresponding linewidth or R_2 relaxation rate in fully hydrated tissues depends on the variance of RDC, i.e., $\langle (P_2(\cos\theta))^2\rangle$. Note, the angle brackets stand for an ensemble or time average.

In the human brain WM, water molecules close to the hydrophilic surface of phospholipid bilayers, as schematically shown in Figure 1A, are highly organized as revealed by an advanced Raman scattering microscopic imaging study.[23] Specifically, the direction of water RDC is parallel to the bilayer surface (Fig. 1B) or perpendicular to the surface normal (green dashed line). As the lipid's long hydrocarbon chains are predominantly aligned with and rapidly rotate around the surface normal (Fig. 1C),[29, 37] the direction of average RDC from lipid's methylene (CH2) groups becomes orthogonal to that from water in WM (Fig. 1B). It is worth mentioning that these *static* RDC configurations are only valid on the timescale of 10^{-14} s, i.e., vibrational frequencies from the pertinent chemical bond stretching modes[23] that are unrelated to proton MR relaxation.[2, 3]

As demonstrated in Figure 2A, a concentric distribution of RDCs around an axon can be rearranged into a specific cylindrically symmetric system with an open angle $\alpha = 90°$. In an imaging voxel from biological tissues, another extreme case with $\alpha \approx 0°$ (Figure 2B) could

bioRxiv preprint doi: https://doi.org/10.1101/2021.09.13.460097; this version posted April 19, 2022. The copyright holder for this preprint (which was not certified by peer review) is the author/funder. All rights reserved. No reuse allowed without permission.

coexist as well in which all RDCs are uniformly orientated along one direction.[38, 39] A general function of orientation-dependent R_2 has been obtained by averaging $(3\cos^2\theta - 1)^2$ in an axially symmetric system.[24, 25] Equations 1 and 2 provide respectively the reformatted[25] and the original[24] functions with pertinent angles defined as before and depicted in Figure 2C. The angle θ, formed between <H-H> and B_0, can be expressed by three different angles α, ε and φ denoting respectively between <H-H> and the symmetry axis $\vec{n}$, between $\vec{n}$ and B_0, and the azimuthal angle of <H-H>. An ensemble or time average must be taken over all φ. A few representative orientation (ε) dependences of R_2 with different α are exemplified in Figure 2D.

$$f(\alpha,\varepsilon) = \frac{1}{4}(3\cos^2\alpha - 1)^2(3\cos^2\varepsilon - 1)^2 + \frac{9}{8}(\sin^4\alpha\,\sin^4\varepsilon + \sin^2 2\alpha\,\sin^2 2\varepsilon) \quad (1)$$

$$f(\alpha,\varepsilon) = \frac{1}{512}(a_0 + a_1\cos 2\varepsilon + a_2\cos 4\varepsilon) \quad (2)$$

Here, the coefficients a_0, a_1 and a_2 in Eq. 2 are respectively defined by 81cos4α+156cos2α+467, 180cos4α+432cos2α+156, and 315cos4α+180cos2α+81 as originally presented by Berendsen.[24] It should be mentioned that Eq. 2 was previously employed for characterizing both isotropic and anisotropic transverse relaxation contributions. In this work, however, $f(\alpha,\varepsilon)$ was used only for modeling anisotropic transverse relaxation.

The orientation information can be obtained by physically rotating WM specimens relative to B_0 for studies ex vivo.[19, 20, 40] Because the first measurement may not start at ε=0°, an angle offset ε_0 has to be introduced into Eq. 1 as recently demonstrated.[41] For studies in vivo, on the other hand, the orientation information must be inferred from DTI.[16, 42] Specifically, relative to B_0, the primary eigenvalue direction of diffusion tensor is *assumed* the predominant orientation of axon bundles within an image voxel.[8, 9] If this assumption is valid, the theoretical R_2 or R_2^* orientation dependence profiles will not be offset whereas the prior measurements

bioRxiv preprint doi: https://doi.org/10.1101/2021.09.13.460097; this version posted April 19, 2022. The copyright holder for this preprint (which was not certified by peer review) is the author/funder. All rights reserved. No reuse allowed without permission.

demonstrated otherwise.[17, 18, 31, 43] Therefore, ε_0 has been incorporated in Eq. 1 for studies in vivo in the current work.

In addition, ε_0 was hypothesized linking directly to the direction of a complete anisotropic translational diffusion. For a typical "zeppelin" diffusion tensor, neither axial ($D_\parallel$) nor radial ($D_\perp$) diffusivity characterizes such an anisotropic diffusion. For convenience, $D_\perp$ was assumed arising solely from an isotropic diffusion, and the direction of the vector difference between $D_\parallel$ and $D_\perp$ could be considered along $\vec{n}$ as depicted in Figure 3B, thus resulting in an angle offset ε_0 when $D_\parallel$ was considered as a reference. If average $D_\parallel$ and $D_\perp$ are available from whole WM, an average ε_0 can be calculated by $\tan^{-1}(D_\perp/D_\parallel)$ and compared with the fitted ε_0 to validate the hypothesis. Even better when voxel-based ε_0 is available and has been accounted for, the measured transverse relaxation orientation dependence should be consistent with the theory, without an angle offset ε_0, if the hypothesis is valid.

To conceptually connect an anisotropic rotational motion with an anisotropic translational diffusion, a standard axially symmetric system (Figure 3A) could be transformed into a cylindrical helix model (Figure 3C). Although sharing the same geometric microstructure, the proposed model is radically different from the previously developed hollow cylinder fiber model (HCFM)[44-46], with the former derived from intramolecular residual dipolar interactions but the latter based on the "susceptibility effect". Further, the proposed model deals exclusively with anisotropic R_2 originating from both within (Fig. 2A) and outside (Fig. 2B) myelin sheaths. When the complete anisotropic translational diffusion is incorporated, the proposed cylindrical helix model has captured the most relevant degrees of molecular motions responsible for the observed shifted orientation-dependent R_2 profiles in WM.

bioRxiv preprint doi: https://doi.org/10.1101/2021.09.13.460097; this version posted April 19, 2022. The copyright holder for this preprint (which was not certified by peer review) is the author/funder. All rights reserved. No reuse allowed without permission.

Mathematically, an open angle α and circular helix parameters, i.e., radius (r) and pitch ($2\pi d$), become connected via the relationship of $\tan\alpha = r/d$. Herein, r could be considered as a sum of an average thickness of myelin sheaths and an average nonmyelinated axon radius. Note, the directions of both translational and rotational molecular motions are considered collinear, pointing to an axon primary axis. Given a fixed length of helix pitch, the helix radius will asymptotically grows as α becomes widened. On the other hand, if a water molecule had been spiraling upward around a typical axon, with translational diffusion coefficient D_a and rotational correlation time τ_b, the helix pitch would have been equal to $\sqrt{2D_a(2\pi\tau_b)}$.

3 | METHODS

Unless otherwise specified, all orientation-dependent transverse relaxation rate profiles, identified by letters in an alphabetical order in Table 1, were extracted from image-based graphs in previous publications using a free online tool (www.graphreader.com), and replotted in the figures (black triangles) herein. The orientations (Φ) associated with the measured R_2 and R_2^* were originally determined by the primary diffusivity direction ($\vec{e}_1$) from DTI relative to the main magnetic field $\vec{B}_0$, i.e., $\cos\Phi = \left(\vec{e}_1 \cdot \vec{B}_0\right)/\left(|\vec{e}_1| \cdot |\vec{B}_0|\right)$, with $\Phi = \varepsilon + \varepsilon_0$ as depicted in Figure 3B. These estimated Φ values were sorted by increasing angles from 0° to 90°, and further averaged within a predefined interval or angular resolution (AR). The highest *b* values used in DTI were also provided in Table 1. R_2 and R_2^* mappings were acquired using conventional Carr-Purcell-Meiboom-Gill (CPMG) spin-echo and gradient-echo sequences, respectively. The original relaxation data were acquired from whole brain WM in vivo on 3T MR systems following the ethical guidelines as stated in the original publications; but the use of

bioRxiv preprint doi: https://doi.org/10.1101/2021.09.13.460097; this version posted April 19, 2022. The copyright holder for this preprint (which was not certified by peer review) is the author/funder. All rights reserved. No reuse allowed without permission.

these extracted data was not reconsented. If not stated otherwise, all concerned relaxation metrics were related to restricted water molecules in WM.

3.1 | Anisotropic R_2 derived from Connectome DTI (Group A)

A public domain high-resolution (i.e., an isotropic voxel size of 760 μm^3) Connectome DTI dataset of one healthy human brain (age=30 years)[47] was utilized for validating the proposed theoretical framework regarding ε_0. More specifically, paired with the associated b=0 (s/mm^2) images, 6 preprocessed data subsets with b=1000 (s/mm^2) and 12 with b=2000 (s/mm^2) were individually analyzed using FSL DTIFIT[48] to generate the following fit parameters: eigenvalues (λ_i) and eigenvectors ($\hat{e}_i$), with $i = 1, 2, 3$; fractional anisotropy (FA); mode of anisotropy (MO);[49] and T2W signals (SO) with b=0 (s/mm^2). Supplementary Figure S1 provides exemplary fits for a rectangular ROI (in black) from corpus callosum as pointed by a red arrow in Figure 4D. The mean of the fits from data subgroup with b=1000 (s/mm^2) or b=2000 (s/mm^2) were used independently for further analysis.

Given a known TE=75ms used in DTI,[47] anisotropic R_2 (denoted by R_2^a) could be readily assessed from T2W signal based on Eq. 3 as demonstrated previously.[50] A similar idea has been exploited lately for separating an isotropic R_2^* component from a single GRE measurement.[51]

$$\ln SO/TE = (\ln S_0/TE - R_2^i) - R_2^a * f(\alpha, \Phi) \qquad (3)$$

Note, SO became S_0 (i.e., apparent proton density) when TE=0 and the term $(\ln S_0/TE - R_2^i)$ was treated as a constant C_0 to be determined by fitting. Both S_0 and R_2^i (i.e., isotropic R_2 component) were reportedly least varied in WM.[4] Within the whole brain, the measured SO values (in a logarithmic scale) from specific voxels possessing a linear (i.e., 0.5<FA<0.9 and 0.5<MO<1.0) diffusion anisotropy were sorted based on the calculated fiber orientations (Φ) and then averaged into 180 different bins ranging from 0° to 90°, i.e., AR=0.5°.

bioRxiv preprint doi: https://doi.org/10.1101/2021.09.13.460097; this version posted April 19, 2022. The copyright holder for this preprint (which was not certified by peer review) is the author/funder. All rights reserved. No reuse allowed without permission.

3.2 | Compartmental anisotropic R_2 from myelin water imaging (Group B)

Anisotropic R_2 orientation dependence profiles of myelin water and intra- and extra-cellular (IE) water were retrieved respectively from Figures 7A and 7B in a recent study of orientation-dependent myelin water imaging.[18] In this work, Figures 6A and 6B replicate the orientation-resolved (AR=5°) compartmental R_2 values, measured from eight healthy volunteers with a mean age of 26 years (range=21-33 years). An interval between two adjacent refocusing pulses in CPMG pulse sequence was 8 ms. The highest *b*-value used in DTI was 700 s/mm^2.

In another prior publication,[52] average axial ($D_{\parallel}$=1.44±0.24 μm^2/ms) and radial ($D_{\perp}$=0.47±0.11 μm^2/ms) diffusivities in WM were reported in Table 1 for an age-matched group at 3T. As defined in Figure 3B, an average ε_0 and its uncertainty $\Delta\varepsilon_0$ were respectively calculated by $\tan^{-1}(1/\rho)$ and $\Delta\rho/(1+\rho^2)$, with $\rho=D_{\parallel}/D_{\perp}$ and $\Delta\rho$ derived from $\Delta D_{\parallel}$ and $\Delta D_{\perp}$ following basic error propagation rules.[53] Note, ρ was listed as 3.33±1.29 (μm^2/ms) in the original paper and used in the calculation in this work. Fractional anisotropy (FA) was also computed[8] and tabulated in Table 1 herein.

3.3 | Anisotropic R_2^* from neonates and adults (Groups C and D)

Orientation-dependent R_2^* profile (AR=0.33°) in WM from 8 term neonates (mean age=40.4±1.1 weeks) was retrieved from Figure 3C in a previous study (Group C)[17] and replotted in Figure 7A herein. The highest *b*-value used in DTI was 700 s/mm^2. The directional diffusivities were also reported in the original paper, i.e., $D_{\parallel}$=1.69±0.03 (μm^2/ms) and $D_{\perp}$=1.06±0.04 (μm^2/ms). In a different study on adult WM,[4] orientation-dependent R_2^* measurements (AR=3°) were performed on a group of 11 healthy female and 5 healthy male subjects with an average age of 43.5 ± 12 years (range: 26–67 years, median: 43 years). An average anisotropic R_2^* profile (age $\geq$ 43 years)

bioRxiv preprint doi: https://doi.org/10.1101/2021.09.13.460097; this version posted April 19, 2022. The copyright holder for this preprint (which was not certified by peer review) is the author/funder. All rights reserved. No reuse allowed without permission.

was retrieved from Figure 2g in the original publication[4] and reproduced in Figure 7B in this work. The highest *b*-value used in DTI was 1000 s/mm^2.

3.4 | Anisotropic T_2^b deduced from semisolid macromolecules in WM (Group E)

qMT imaging was performed on 7 healthy subjects (mean age=26 years, range=19–33 years).[31] The system characteristic MT parameters were determined based on a two-compartment model comprising a liquid pool of free water and a semisolid pool of macromolecules. The derived average transverse relaxation time T_2^b orientation dependence profiles of semisolid macromolecules in WM were retrieved from Figure 7a in the original paper and replicated in Figure 7C in this work. The highest *b*-value used in DTI was 1000 s/mm^2. The reported proton T_2^b was largely associated with semisolid methylene (CH2) groups on lipid hydrocarbon chains in the interior of lipid bilayers in WM.[31]

3.5 | Anisotropic R_2^* from people with MS and two controls (Group F)

A clinical study of anisotropic R_2^* orientation dependences in WM was conducted among people with multiple sclerosis (MS, n=39; mean age=49.7±10.1 years), their age-matched asymptomatic siblings (SBL, n=28) and unrelated healthy controls (CNT, n=27).[32] Anisotropic R_2^* profiles (AR=5°) of each subject from three groups were retrieved from Supporting Information in the original paper, and group-average R_2^* profiles were presented in Figure 8A herein. The highest *b*-value used in DTI was 1000 s/mm^2.

3.6 | Nonlinear least-squares curve fittings

An optimization method of Levenberg-Marquardt nonlinear least-squares, implemented in an IDL script from the public domain (http://purl.com/net/mpfit),[54] was used for modeling anisotropic R_2 and R_2^* orientation dependence profiles, based on the proposed model ($R_{2,1}$) in Eq. 4, herein referred to as “Fit A”.

bioRxiv preprint doi: https://doi.org/10.1101/2021.09.13.460097; this version posted April 19, 2022. The copyright holder for this preprint (which was not certified by peer review) is the author/funder. All rights reserved. No reuse allowed without permission.

$$R_{2,1} = R_2^i + R_2^a * f(\alpha, \Phi - \varepsilon_0) \quad (4)$$

$$R_{2,2} = b_0 - b_1 \cos 2\Phi + b_2 \cos 4\Phi \quad (5)$$

$$R_{2,3} = R_2^i + R_2^a * f(90°, \Phi) \quad (6)$$

There were four model parameters and one independent variable (Φ) in Eq. 4, i.e., R_2^i and R_2^a denoting orientation independent and dependent contributions, an open angle α for a particular RDC distribution, and an angle offset ε_0. The same data from some Groups were also fitted using a previously developed model $R_{2,2}$ (without ε_0) as written in Eq. 5 (labeled as "Fit B"). It should be emphasized that when Fit B included ε_0, it would become equivalent to Fit A albeit with different model parameters. With α fixed to 90° and ε_0 set to 0°, $R_{2,1}$ was transformed into $R_{2,3}$ (Eq. 6), referred to as "Fit C". For consistency, T2W signal fitting in Eq. 3 was categorized in the same way as in Eq. 4, i.e., referred to as either "Fit A" or "Fit B" with or without ε_0 in $f(\alpha, \Phi)$, respectively.

Initiating with five sets of different values within different constraints, the curve fittings were unweighted and constrained, [55] with the limited ranges for model parameters: C_0=[50, 200]; R_2^i=b_0=[0, 100] (1/s); R_2^a=b_1=[0, 50] (1/s); α=[0°, 90°]; ε_0=[-45°, 45°]; and b_2=[0, 10] (1/s). Note, T_2^b in units of μs from Group E was converted into R_2^b (=1/T_2^b) and then scaled down within the scale of fitting parameter constraints. Goodness of fit was characterized by root-mean-square error (RMSE), based on the measured ("Exp") and fitted ("Fit") transverse relaxation orientation dependence profiles (represented by N data points), i.e., $\sqrt{\sum_i (Exp_i - Fit_i)^2/N}$, with i changing from 1 to N. The statistical significance was assessed by an F-test when comparing two fitting models. A P-value was derived from F-distributions with significance indicated by $P \leq 0.05$.

bioRxiv preprint doi: https://doi.org/10.1101/2021.09.13.460097; this version posted April 19, 2022. The copyright holder for this preprint (which was not certified by peer review) is the author/funder. All rights reserved. No reuse allowed without permission.

All the reported fitting results (mean ± standard deviation) were obtained from Fit A unless specified otherwise. Pearson correlation coefficients (PCC) were listed in Table 2 between the fits from Group F and the age of each participant from individual or combined subgroups. The statistical significance of observed linear correlations was also set to $P \leq 0.05$. All image and data analysis were performed using customized codes written in IDL 8.8 (Harris Geospatial Solutions, Broomfield, CO, USA).

4 | RESULTS

4.1 | Anisotropic R_2 orientation dependence with an offset

Figure 4 presents four parametric maps derived from DTI (b=1000 s/mm^2): (A) $C_0 - \ln(SO)/TE$, an equivalent of anisotropic R_2, (C) orientations (i.e., $\Phi = \varepsilon + \varepsilon_0$) of principal diffusivities, (D) modes of anisotropies ranging from 1.0 to -0.1 denoting respectively an ideally linear ("stick") and an ideally planar ("plate") diffusion tensor, and (F) colored fractional anisotropies (i.e., $\vec{e}_1$*FA). An anisotropic R_2 orientation dependence profile was plotted (B) as a ribbon (width=mean ± SD, n=6). The image voxels from whole brain WM were selected according to limited FA and MO ranges as highlighted (black box) in 2D histogram (E). An ROI-based (pointed by a red arrow in Fig. 4D) average fits (mean ± SD) from all data subsets (n=18) for different parameters are plotted in Supplementary Figure S1 including three diffusivities (λ_i, $i = 1.2.3$) and mean diffusivity (MD). Although derived from T2W images with a single TE, this characteristic profile was comparable to the previous in healthy adult human brains based on the standard T_2 mapping with multiple varying TEs.

Figure 5 demonstrates the fitted anisotropic R_2 profiles using Fit A (red solid lines) and Fit B (blue dashed lines) before (A and D) and after (C and F) correcting voxel-based angle

bioRxiv preprint doi: https://doi.org/10.1101/2021.09.13.460097; this version posted April 19, 2022. The copyright holder for this preprint (which was not certified by peer review) is the author/funder. All rights reserved. No reuse allowed without permission.

offset ε_0 derived from diffusivities with b=1000 s/mm^2 (A-C) or b=2000 s/mm^2 (D-F). Fit A significantly (P<0.01) outperformed Fit B without the voxel-based ε_0 corrections; however, the differences between the two fits disappeared after correcting the voxel-based ε_0. For data with b=1000 s/mm^2, for instance, before and after the corrections. the calculated RMSEs between Fit A and Fit B were 0.081 vs. 0.137 and 0.081 vs. 0.081, respectively.

The voxel-based ε_0 orientation dependences are profiled (mean ± SD) for DTI data with b=1000 s/mm^2 (B) and b=2000 s/mm^2 (E), showing that the fitted ε_0 (vertical dashed lines, 15.2° ± 4.9°, A; 16.0° ± 2.9, D) and the calculated average $\langle\varepsilon_0\rangle$ (horizontal dashed lines, 15.8° ± 0.2°, B; 17.9° ± 0.2°, E) become equivalent within the measurement errors. Although consistent with previous findings, the fitted R_2^a (1/s) based on low b-value data (C) was substantially smaller (i.e., 2.6 ± 0.6 vs. 4.5 ± 0.6) than that with high b-value (F) on the same subject even after the ε_0 corrections.

4.2 | Anisotropic R_2 from myelin water imaging

Figure 6 reveals that Fit A significantly (P < 0.01) outperformed Fit B for characterizing anisotropic R_2 profiles (black triangles) of myelin water (A) and intra- and extra-cellular (IE) water (B) based on Group B data,[18] indicated by reduced fitting residuals (i.e., ΔR_2=Fit-Exp, C and D). Quantitatively, the calculated RMSEs from Fit A, relative to those from Fit B, decreased almost half for myelin water (i.e., 0.350 vs. 0.724) and IE water (i.e., 0.011 vs. 0.021).

Between the two partitioned water pools, the fitted α (i.e., 67.0±0.6° vs. 69.0±0.2°) and ε_0 (i.e., 15.2±1.1° vs. 16.1±0.9°) were comparable despite markedly different R_2^i (1/s) (i.e., 76.3±0.6 vs. 13.8±0.0) and R_2^a (1/s) (i.e., 16.1±0.8 vs. 1.0±0.0). On the other hand, the calculated ε_0 (i.e., 16.7±6.1°) based on average directional diffusivities in highly anisotropic (i.e., FA=0.60±0.12) WM was comparable with the fitted ε_0 from anisotropic R_2 profiles as expected.

bioRxiv preprint doi: https://doi.org/10.1101/2021.09.13.460097; this version posted April 19, 2022. The copyright holder for this preprint (which was not certified by peer review) is the author/funder. All rights reserved. No reuse allowed without permission.

4.3 | Anisotropic R_2^* in WM from neonates and adults

Whereas both were better modeled using Fit A than using Fit B, the observed anisotropic R_2^* profile of neonates (Figure 7A) was substantially different from that of adults (Figure 7B). Specifically, the fits were smaller from neonates than from adults for R_2^i (1/s), i.e., 7.2±0.1 vs. 15.9±0.1; R_2^a (1/s), i.e., 1.3±0.1 vs. 5.1±0.1, and α (°), i.e., 38.1±0.4 vs. 70.0±0.1, but became larger for ε_0 (°), i.e., 38.5±0.3 vs. 16.9±0.4 (vertical dashed green lines, A and B). The fitted ε_0 (°) from neonates was slightly larger than the calculated counterpart (i.e., 38.5±0.3 vs. 32.1±1.1), probably due to an inaccurate replication of scattered R_2^* data from the original graph. Nonetheless, neonates possessed less anisotropic WM when compared with adults as indicated by the reported FAs (see Table 1). It is worth noting that a relatively reduced R_2^* in neonatal WM stemmed largely from an anisotropic component and R_2 was reportedly independent of B_0 that is in good agreement with the proposed theoretical framework.[56]

4.4 | Anisotropic T_2^b of semisolid CH2 in WM from adults

As demonstrated in Figures 7C and 7F, the profile of qMT-derived T_2^b (i.e., $1/R_2^b$) from image voxels with FA > 0.7 was significantly ($P < 0.01$) better modeled using Fit A than using Fit C. Despite originating from distinct proton groups and imaging methods, the fitted α (~70°) appeared surprisingly close to that found in other adult groups as listed in Table 1. However, the fitted ε_0 (°) was nearly twofold bigger than that from water proton R_2^* profile as shown in Figure 7B. Although consistent with the semisolid nature, the fitted R_2^i and R_2^a were unexpectedly higher (i.e., ~50x10^3 1/s) when compared to the previously reported resonance linewidth of lipid chain protons from non-orientated bilayers, i.e., ~3-6 kHz.[57]

4.5 | Anisotropic R_2^* in WM with multiple sclerosis (MS)

bioRxiv preprint doi: https://doi.org/10.1101/2021.09.13.460097; this version posted April 19, 2022. The copyright holder for this preprint (which was not certified by peer review) is the author/funder. All rights reserved. No reuse allowed without permission.

Figure 8A shows average anisotropic R_2^* orientation dependence profiles for multiple sclerosis (MS, red), age-matched siblings (SBL, green) and unrelated healthy control (CNT, blue) groups. Although the fitted α and ε_0 were comparable as shown by colored imprints (Figure 8A), the fitted R_2^a became the lowest for MS subgroup (Figure 8B) and so was R_2^i but to less degree. Figures 8C-F display scatterplots between individual ages and the corresponding fits of R_2^i, R_2^a, α, and ε_0 from three subgroups, overlaid respectively with a 95% confidence ellipse.

Compared to those from two controls, R_2^i and R_2^a from MS subgroup were reduced but ε_0 increased. Linear regression lines from combined subgroups were also included, highlighting significant ($P \leq 0.05$) positive (PCC = 0.38 for R_2^i) and negative (PCC = -0.20 and -0.23 for R_2^a and α, respectively) correlations, as tabulated in Table 2, between aging (or demyelination) and the fits. The fitted ε_0 more or less (PCC = 0.11, P=0.28) followed the similar trend of R_2^i. In general, an older people most likely possessed increased R_2^i and ε_0 but decreased R_2^a and α, in accordance with what had been known in neonates with developing WM (Figure 7A).

5 | DISCUSSION

5.1 | A cylindrical helix model for molecular rotation and translation

This work proposed a unique cylindrical helix model for characterizing anisotropic proton transverse relaxation orientation dependences in the human brain WM at 3T. This model shares some remarkable similarities with its predecessors.[14, 20, 21, 31] First, the ultrastructure of myelin is described as multiple layers of lipid bilayers spiraling around an axon and further considered as the source of orientation-dependent transverse relaxation. Second, the most relevant direction is the orientation of an axon fiber, rather than individual directions of molecular constituents distributed around the axon. Third, other macromolecules such as membrane proteins in bilayers

bioRxiv preprint doi: https://doi.org/10.1101/2021.09.13.460097; this version posted April 19, 2022. The copyright holder for this preprint (which was not certified by peer review) is the author/funder. All rights reserved. No reuse allowed without permission.

are ignored. Nevertheless, the proposed model possesses several unusual characteristics with respect to prior models.

First, it brings together anisotropic R_2 and DTI diffusivities by an angle offset ε_0. To our knowledge, this is the first time to combine the most relevant degrees of molecular motions for characterizing highly organized microstructures in WM.[26, 28] Second, this proposed model is a generalized MAE model,[24, 25] applied to not only ordered "liquid-like" water on the surface but also dynamic "solid-like" CH2 protons in the interior of bilayers. Further, it can be also used in peripheral nervous system, not to mention other tissues,[25] where ordered water seemed uniformly ($\alpha \approx 0°$) aligned in elongated collagenous tissues as shown in Supplementary Figure S2.[58] Third, this generalized model is built upon residual dipolar interactions,[24, 25] fundamentally different from those based on tensorial magnetic susceptibility. Theoretically,[14] the susceptibility-induced proton transverse relaxation rate is quadratically scaled with the strength of B_0; as a result, this relaxation pathway will become more relevant only at a higher B_0. As shown in Supplementary Figure S3, the susceptibility-induced contribution to the total relaxation rate was about 5% at 3T, based on B_0 dependent $R_{1\rho}$ dispersion data on rat brain.[59] This theoretical prediction has been corroborated by the previous in vivo study showing that R_2 from neonatal brain WM was principally independent of B_0 ranging from 1.0T to 3.0T.[56] These theoretical and experimental results have justified the relaxation mechanism underlying the proposed model, in excellent agreement with the previous finding in knee articular cartilage.[36, 60]

5.2 | An angle offset ε_0 depending on directional diffusivities

Initially, an angle offset ε_0 was introduced as an ansatz for better modeling R_2 orientation dependences in WM.[41] Based on a high resolution Connectome DTI dataset,[47] we provided strong evidence that ε_0 is indeed modulated by DTI diffusivities although the detailed

bioRxiv preprint doi: https://doi.org/10.1101/2021.09.13.460097; this version posted April 19, 2022. The copyright holder for this preprint (which was not certified by peer review) is the author/funder. All rights reserved. No reuse allowed without permission.

mathematical functions for related anisotropic molecular motions need to be constructed. As shown in Figure 5, the previously reported R_2 would have relatively larger measurement uncertainties when close to "zero" degrees due to the low number of voxels possessing such orientations. To throw away these valuable yet imprecise data points would not be good practice as it could conceal the critical information underlying the actual biophysical mechanism.[43]

The fitted average $\langle\varepsilon_0\rangle$ and R_2^a as shown in Figure 5 were larger when using a higher *b*-value in DTI. This result can be ascribed to decreased FA, stemmed mostly from reduced $D_\parallel$ for a zeppelin tensor as demonstrated in Supplementary Figure S1. Therefore, $\langle\varepsilon_0\rangle$ became larger based on the relationship $\tan\varepsilon_0 = D_\perp/D_\parallel$ (see Figure 3B). Because of the fixed voxel selection criterion (i.e., 0.5 < FA < 0.9) regardless of *b*-values, more image voxels with relatively higher FA were included in constructing R_2 profiles with higher *b*-values, resulting in an enhanced R_2^a relative to that with lower *b*-values as demonstrated. These results suggest that some caution should be exercised when comparing previously reported R_2 orientation dependence profiles. This important point has been clearly demonstrated in Figure 5 in the literature.[31]

Nonetheless, the fitted ε_0 from previous transverse relaxation orientation dependences showed an increasing trend with aging in elderly (Figure 8F), consistent with an increasing ε_0 from healthy adults to neonates (Figures 7A and 7B). These findings imply that ε_0, or $D_\perp/D_\parallel$, appeared to be modulated by an extent of myelination in WM, in good agreement with the literature in which an increased myelination was linked to a decreased $D_\perp$.[61] In an extreme scenario, ε_0 can be zero if anisotropic R_2 is induced exclusively by oriented water on the surface (i.e., α=90°) of lipid bilayers. With the absence of myelin in newborns,[62] ε_0 can also become zero in WM, corresponding to an ideal intra-axonal compartment with $D_\perp$ normally set to zero.[7,

bioRxiv preprint doi: https://doi.org/10.1101/2021.09.13.460097; this version posted April 19, 2022. The copyright holder for this preprint (which was not certified by peer review) is the author/funder. All rights reserved. No reuse allowed without permission.

The fitted ε_0 from anisotropic T_2^b of semisolid CH2 protons (Figure 7C) deserves further explanation. The reported T_2^b orientation dependence was guided by the direction inferred from the diffusion of water rather than lipid molecules. Moreover, lipid hydrocarbon chains may not be perfectly orientated along the bilayer normal as assumed (Figure 1B) particularly for more complex membranes that are rich in cholesterol (such as myelin).[63] Hence, it is not surprising that the discrepancy appeared in the fitted ε_0 as shown between Figures 7B and 7C.

5.3 | An angle α for specific RDC distributions

A general form of MAE function $f(\alpha, \varepsilon)$ as written in Eq. 1 can be thought as a combination of two extreme cases, i.e., $f(0°, \varepsilon)$ and $f(90°, \varepsilon)$, with different weighting indicated by an open angle α. If observed anisotropic transverse relaxation in WM had resulted exclusively from ordered water within myelin multiple layers, the fitted α would have become 90° as shown in Figure 2A. The actual fitted α was, however, close to 70° for adult brain WM based on either ordered water or semisolid CH2 proton R_2 relaxation measurements. This result implies that some uniformly aligned (i.e., α=0°) RDCs, at least from ordered water, had made considerably contributions. Previously published studies showed that these contributions increased as myelination decreased in WM of neonates[17] until they completely dominated when myelin was absent in WM of newborns.[62] This argument might help us to understand the reported increased R_2 anisotropy in the very preterm infant brain when compared with that from the late preterm infant brain.[64]

For spins on lipid chains, D_a=4*10^{-3} (μm^2/ms) and τ_b=100 (ms/rad) were reported[65] and d=0.36μm could be determined based on the proposed model (Figure 3C) using the equation $2\pi d=\sqrt{2D_a(2\pi\tau_b)}$. Further, an open angle of α could be determined to be approximately 70°, close to the findings from this work, if the radius of a representative axon is assumed 1.0 μm.[66]

bioRxiv preprint doi: https://doi.org/10.1101/2021.09.13.460097; this version posted April 19, 2022. The copyright holder for this preprint (which was not certified by peer review) is the author/funder. All rights reserved. No reuse allowed without permission.

To match the same α for restricted water, D_a=2.0 (μm^2/ms)[27] and τ_b=0.2 (ms/rad) ought to be expected. Whereas the value of D_a for restricted water seems not unreasonable in WM in vivo, the value of τ_b is uncertain.[46, 67] More research is thus warranted.

5.4 | Isotropic R_2 relaxation contributions

According to Eq. 4, the observed proton MR transverse relaxation rates were divided into isotropic (R_2^i) and anisotropic (R_2^a) components, essentially assuming fast spin exchange between two environments.[68] The former may arise from several relaxation pathways such as intrinsic dipolar interactions modulated by fast (e.g., pico- and nanoseconds) timescales of molecular motions,[2, 50] chemical exchange and diffusion due to slow (e.g., micro- and milliseconds) molecular motions,[46] and non-local magnetic susceptibility inhomogeneity (R_2') if gradient echo rather than spin echo signal was used.[20] Contrast to the intrinsic dipolar interactions on fast timescales, the effect of slow molecular motions on R_2^i can be suppressed by $R_{1\rho}$ dispersion.[46, 69]

The fitted R_2^i was reduced in developing (Figure 7A) and pathological (Figure 8C) WM compared to that in the healthy brain, consistent with fewer macromolecular labile protons. It was also shown[41] that R_2^i was considerably larger at ≥7T ex vivo when compared to those at 3T in vivo, possibly due to an increased B_0 inhomogeneity. Interestingly, The fitted R_2^i from the sibling control group was relatively higher than that from the MS group (Figure 8C), originally ascribed to an excess iron deposition as a predisposition for MS.[32] As iron-induced transverse relaxation appears orientation-independent,[20] it is thus essential to accurately separate R_2^i from R_2^a based on a reliable biophysical model for a meaningful evaluation of iron deposition in WM.[70]

5.5 | Anisotropic R_2 relaxation component

bioRxiv preprint doi: https://doi.org/10.1101/2021.09.13.460097; this version posted April 19, 2022. The copyright holder for this preprint (which was not certified by peer review) is the author/funder. All rights reserved. No reuse allowed without permission.

For an anisotropic contribution, its maximum could be $4R_2^a$ as if all the relevant RDCs become consistently orientated along B_0, i.e., $f(0°, 0°)$=4. The observed R_2^a relied on not only the amount of RDCs but also the degree of their restricted molecular motions. For instance, a relatively decreased R_2^a was found in neonatal developing WM (Figure 7A) and compromised WM from people with MS (Figure 8B). Perhaps, an extreme "demyelination" case would be elongated cellular constituents (e.g., microtubules and neurofilaments) in an intra-axonal space, revealing a considerably reduced R_2^a compared to that in an extra-axonal space as shown in Supplementary Figure S4.[7] On the other hand, a considerably increased R_2^a was measured at room temperatures on formalin-fixed WM specimens embedded in an agarose gel at higher fields (≥7T).[40, 41] Moreover, the measured R_2^a from semisolid CH2 groups in WM was much larger than that from dynamically ordered water close to the phospholipid bilayer surface (Table 1).

It should be clarified that previously published T_2^b (i.e., ~10-15 μs) from qMT imaging may not be directly linked to the measured CH2 proton resonance absorption linewidth $\Delta\nu$ (i.e., ~3-6 kHz) via the relationship of $\Delta\nu = 1/\pi\, T_2^b$, commonly used in an isotropic solution.[57, 71] Thus, it may not be appropriate to interpret the fitted R_2^i and R_2^a in the same way as those found from their water counterparts. It has been shown before that the same qMT imaging data from bovine WM specimen could be fitted using either Lorentzian (T_2^b=230±20 μs) or Super Lorentzian (T_2^b=10.4±0.5 μs) line shape for semisolid protons, albeit with a reduced fitting error for the latter line shape.[72] If a similar scaling factor (~25) had been incorporated into the fitted R_2^i and R_2^a in this work, these values would have been scaled down to the order of kHz as expected. Nonetheless, based on the comparable fitted R_2^i and R_2^a, we can conclude that about 80% of T_2^b originated from orientation-dependent semisolid CH2 protons in WM, i.e., $4R_2^a/\left(R_2^i + 4R_2^a\right) \approx 0.8$.

bioRxiv preprint doi: https://doi.org/10.1101/2021.09.13.460097; this version posted April 19, 2022. The copyright holder for this preprint (which was not certified by peer review) is the author/funder. All rights reserved. No reuse allowed without permission.

6 | CONCLUSIONS

In summary, a cylindrical helix model, encompassing both anisotropic molecular translation and rotation, has been proposed for orientation-dependent proton transverse relaxation in the human brain white matter. This proposed general model can better characterize previously published anisotropic transverse relaxation profiles from various physiological and pathological conditions, thereby providing further insight into myelin microstructural alterations at the molecular level.

ACKNOWLEDGEMENTS

The author is very grateful to Dr. Harald E. Möller (Max Planck Institute for Human Cognitive and Brain Sciences, Leipzig, Germany) for his insightful comments and constructive criticisms, and to Dr. Vladimír Mlynárik (Medical University of Vienna, Vienna, Austria) for his valuable suggestions on the earlier versions of this manuscript. The author would also like to thank Dr. Fuyixue Wang (Massachusetts General Hospital, Charlestown, MA, USA) and Dr. Enedino Hernández-Torres (University of British Columbia, Vancouver, Canada) for sharing Connectome DTI and clinical anisotropic R_2^* data in public domains.

DATA AVAILABILITY STATEMENT

Data used in this work are available on request from the author.

ORCID

Yuxi Pang: https://orcid.org/0000-0001-5039-0236

REFERENCES

bioRxiv preprint doi: https://doi.org/10.1101/2021.09.13.460097; this version posted April 19, 2022. The copyright holder for this preprint (which was not certified by peer review) is the author/funder. All rights reserved. No reuse allowed without permission.

1. Chávez FV, Halle B. Molecular basis of water proton relaxation in gels and tissue. *Magn Reson Med*. 2006;56(1):73-81.
2. Knispel RR, Thompson RT, Pintar MM. Dispersion of proton spin-lattice relaxation in tissues. *J Magn Reson*. 1974;14(1):44-51.
3. Persson E, Halle B. Cell water dynamics on multiple time scales. *Proc Natl Acad Sci USA*. 2008;105(17):6266-6271.
4. Schyboll F, Jaekel U, Weber B, Neeb H. The impact of fibre orientation on T 1-relaxation and apparent tissue water content in white matter. *Magnetic Resonance Materials in Physics, Biology and Medicine*. 2018;31(4):501-510.
5. Schyboll F, Jaekel U, Petruccione F, Neeb H. Origin of orientation‐dependent R1 (= 1/T1) relaxation in white matter. *Magnet Reson Med*. 2020;84(5):2713-2723.
6. Lee J, Nam Y, Choi JY, Kim EY, Oh SH, Kim DH. Mechanisms of T2* anisotropy and gradient echo myelin water imaging. *NMR Biomed*. 2017;30(4):e3513.
7. Tax CMW, Kleban E, Chamberland M, Baraković M, Rudrapatna U, Jones DK. Measuring compartmental T(2)-orientational dependence in human brain white matter using a tiltable RF coil and diffusion-T(2) correlation MRI. *Neuroimage*. 2021;236:117967.
8. Basser PJ, Pierpaoli C. Microstructural and physiological features of tissues elucidated by quantitative-diffusion-tensor MRI. *J Magn Reson*. 2011;213(2):560-570.
9. Beaulieu C. The biological basis of diffusion anisotropy. *Diffusion MRI*. Elsevier; 2014:155-183.
10. Le Bihan D, Mangin JF, Poupon C, et al. Diffusion tensor imaging: concepts and applications. *J Magn Reson Imaging*. 2001;13(4):534-546.
11. Dibb R, Liu C. Joint eigenvector estimation from mutually anisotropic tensors improves susceptibility tensor imaging of the brain, kidney, and heart. *Magnet Reson Med*. 2017;77(6):2331-2346.
12. Bao L, Xiong C, Wei W, Chen Z, van Zijl PC, Li X. Diffusion-regularized susceptibility tensor imaging (DRSTI) of tissue microstructures in the human brain. *Medical image analysis*. 2021;67:101827.
13. Wisnieff C, Liu T, Spincemaille P, Wang S, Zhou D, Wang Y. Magnetic susceptibility anisotropy: cylindrical symmetry from macroscopically ordered anisotropic molecules and accuracy of MRI measurements using few orientations. *Neuroimage*. 2013;70:363-376.
14. Wharton S, Bowtell R. Gradient echo based fiber orientation mapping using R2* and frequency difference measurements. *Neuroimage*. 2013;83:1011-1023.
15. Georgiadis M, Schroeter A, Gao Z, et al. Nanostructure-specific X-ray tomography reveals myelin levels, integrity and axon orientations in mouse and human nervous tissue. *Nature communications*. 2021;12(1):1-13.
16. Denk C, Torres EH, MacKay A, Rauscher A. The influence of white matter fibre orientation on MR signal phase and decay. *NMR Biomed*. 2011;24(3):246-252.
17. Weber AM, Zhang Y, Kames C, Rauscher A. Myelin water imaging and R2* mapping in neonates: Investigating R2* dependence on myelin and fibre orientation in whole brain white matter. *NMR Biomed*. 2020;33(3):e4222.
18. Birkl C, Doucette J, Fan M, Hernandez-Torres E, Rauscher A. Myelin water imaging depends on white matter fiber orientation in the human brain. *Magn Reson Med*. 2021;85(4):2221-2231.
19. Lee J, van Gelderen P, Kuo L-W, Merkle H, Silva AC, Duyn JH. T2*-based fiber orientation mapping. *Neuroimage*. 2011;57(1):225-234.

bioRxiv preprint doi: https://doi.org/10.1101/2021.09.13.460097; this version posted April 19, 2022. The copyright holder for this preprint (which was not certified by peer review) is the author/funder. All rights reserved. No reuse allowed without permission.

20. Oh S-H, Kim Y-B, Cho Z-H, Lee J. Origin of B0 orientation dependent R2*(= 1/T2*) in white matter. *Neuroimage*. 2013;73:71-79.
21. Knight MJ, Dillon S, Jarutyte L, Kauppinen RA. Magnetic resonance relaxation anisotropy: Physical principles and uses in microstructure imaging. *Biophysical journal*. 2017;112(7):1517-1528.
22. Knight MJ, Wood B, Couthard E, Kauppinen R. Anisotropy of spin-echo T2 relaxation by magnetic resonance imaging in the human brain in vivo. *Biomedical Spectroscopy and Imaging*. 2015;4(3):299-310.
23. Cheng J-X, Pautot S, Weitz DA, Xie XS. Ordering of water molecules between phospholipid bilayers visualized by coherent anti-Stokes Raman scattering microscopy. *Proc Natl Acad Sci USA*. 2003;100(17):9826-9830.
24. Berendsen HJC. Nuclear magnetic resonance study of collagen hydration. *J Chem Phys*. 1962;36(12):3297-3305.
25. Pang Y. Characterization of anisotropic T2W signals from human knee femoral cartilage: The magic angle effect on a spherical surface. *NMR Biomed*. 2021;34(7):e4535.
26. Novikov DS, Kiselev VG, Jespersen SN. On modeling. *Magnet Reson Med*. 2018;79(6):3172-3193.
27. Veraart J, Novikov DS, Fieremans E. TE dependent Diffusion Imaging (TEdDI) distinguishes between compartmental T2 relaxation times. *NeuroImage*. 2018;182:360-369.
28. Slator PJ, Palombo M, Miller KL, et al. Combined diffusion‐relaxometry microstructure imaging: Current status and future prospects. *Magnet Reson Med*. 2021;86(6):2987-3011.
29. Bloom M, Burnell EE, MacKay AL, Nichol CP, Valic MI, Weeks G. Fatty acyl chain order in lecithin model membranes determined from proton magnetic resonance. *Biochemistry*. 1978;17(26):5750-5762.
30. Watnick PI, Dea P, Chan SI. Characterization of the transverse relaxation rates in lipid bilayers. *Proc Natl Acad Sci USA*. 1990;87(6):2082-2086.
31. Pampel A, Müller DK, Anwander A, Marschner H, Möller HE. Orientation dependence of magnetization transfer parameters in human white matter. *Neuroimage*. 2015;114:136-146.
32. Hernández-Torres E, Wiggermann V, Hametner S, et al. Orientation dependent MR signal decay differentiates between people with MS, their asymptomatic siblings and unrelated healthy controls. *Plos One*. 2015;10(10):e0140956.
33. Mathur-De Vre R. The NMR studies of water in biological systems. *Progress in Biophysics and Molecular Biology*. 1980;35:103-134.
34. Woessner DE. Nuclear magnetic-relaxation and structure in aqueous heterogenous systems. *Mol Phys*. 1977;34(4):899-920.
35. Lenk R, Bonzon M, Greppin H. Dynamically oriented biological water as studied by NMR. *Chemical Physics Letters*. 1980;76(1):175-177.
36. Pang Y. An order parameter without magic angle effect (OPTIMA) derived from R1ρ dispersion in ordered tissue. *Magn Reson Med*. 2020;83(5):1783-1795.
37. Wennerström H. Proton nuclear magnetic resonance lineshapes in lamellar liquid crystals. *Chemical Physics Letters*. 1973;18(1):41-44.
38. Bydder M, Rahal A, Fullerton GD, Bydder GM. The magic angle effect: a source of artifact, determinant of image contrast, and technique for imaging. *J Magn Reson Imaging*. 2007;25(2):290-300.
39. Grunder W. MRI assessment of cartilage ultrastructure. *NMR Biomed*. 2006;19(7):855-876.

bioRxiv preprint doi: https://doi.org/10.1101/2021.09.13.460097; this version posted April 19, 2022. The copyright holder for this preprint (which was not certified by peer review) is the author/funder. All rights reserved. No reuse allowed without permission.

40. Aggarwal M, Kageyama Y, Li X, Van Zijl PC. B0‐orientation dependent magnetic susceptibility‐induced white matter contrast in the human brainstem at 11.7 T. *Magnet Reson Med*. 2016;75(6):2455-2463.
41. Pang Y. Anisotropic transverse relaxation in the human brain white matter induced by restricted rotational diffusion. In: Proceedings of the International Society of Magnetic Resonance Medicine, Virtual, 2021:1711.
42. Bender B, Klose U. The in vivo influence of white matter fiber orientation towards B0 on T2* in the human brain. *NMR Biomed*. 2010;23(9):1071-1076.
43. Doucette J, Wei L, Hernandez-Torres E, et al. Rapid solution of the Bloch-Torrey equation in anisotropic tissue: Application to dynamic susceptibility contrast MRI of cerebral white matter. *Neuroimage*. 2019;185:198-207.
44. Wharton S, Bowtell R. Fiber orientation-dependent white matter contrast in gradient echo MRI. *Proc Natl Acad Sci USA*. 2012;109(45):18559-18564.
45. Hédouin R, Metere R, Chan K-S, et al. Decoding the microstructural properties of white matter using realistic models. *NeuroImage*. 2021;237:118138.
46. Adelnia F, Zu Z, Spear JT, Weng F, Harkins KD, Gore JC. Tissue characterization using R1rho dispersion imaging at low locking fields. *Magnetic Resonance Imaging*. 2021;84:1-11.
47. Wang F, Dong Z, Tian Q, et al. In vivo human whole-brain Connectom diffusion MRI dataset at 760 μm isotropic resolution. *Scientific Data*. 2021;8(1):1-12.
48. Smith SM, Jenkinson M, Woolrich MW, et al. Advances in functional and structural MR image analysis and implementation as FSL. *Neuroimage*. 2004;23:S208-S219.
49. Ennis DB, Kindlmann G. Orthogonal tensor invariants and the analysis of diffusion tensor magnetic resonance images. *Magn Reson Med*. 2006;55(1):136-146.
50. Pang Y, Palmieri-Smith RM, Malyarenko DI, Swanson SD, Chenevert TL. A unique anisotropic R2 of collagen degeneration (ARCADE) mapping as an efficient alternative to composite relaxation metric (R2 -R1 rho) in human knee cartilage study. *Magn Reson Med*. 2019;81(6):3763-3774.
51. Papazoglou S, Streubel T, Ashtarayeh M, et al. Biophysically motivated efficient estimation of the spatially isotropic component from a single gradient‐recalled echo measurement. *Magnet Reson Med*. 2019;82(5):1804-1811.
52. Mädler B, Drabycz SA, Kolind SH, Whittall KP, MacKay AL. Is diffusion anisotropy an accurate monitor of myelination?: Correlation of multicomponent T2 relaxation and diffusion tensor anisotropy in human brain. *Magnetic resonance imaging*. 2008;26(7):874-888.
53. Bevington PR, Robinson DK. *Data reduction and error analysis for the physical sciences*. 3rd ed. McGraw-Hill; 2003.
54. Markwardt CB. In: Bohlender D, Dowler P, Durand D, eds. Proceedings of Astronomical Data Analysis Software and Systems XVIII, Quebec, Canada, ASP Conference Series, Vol. 411. San Francisco, CA: Astronomical Society of the Pacific; 2009:251-254.
55. Ahearn TS, Staff RT, Redpath TW, Semple SIK. The use of the Levenberg–Marquardt curve-fitting algorithm in pharmacokinetic modelling of DCE-MRI data. *Physics in Medicine & Biology*. 2005;50(9):N85.
56. Williams L-A, Gelman N, Picot PA, et al. Neonatal brain: regional variability of in vivo MR imaging relaxation rates at 3.0 T—initial experience. *Radiology*. 2005;235(2):595-603.
57. Seiter C, Chan SI. Molecular motion in lipid bilayers. Nuclear magnetic resonance line width study. *Journal of the American Chemical Society*. 1973;95(23):7541-7553.

bioRxiv preprint doi: https://doi.org/10.1101/2021.09.13.460097; this version posted April 19, 2022. The copyright holder for this preprint (which was not certified by peer review) is the author/funder. All rights reserved. No reuse allowed without permission.

58. Kästel T, Heiland S, Bäumer P, Bartsch A, Bendszus M, Pham M. Magic angle effect: a relevant artifact in MR neurography at 3T? *American journal of neuroradiology*. 2011;32(5):821-827.
59. Mäkelä HI, De Vita E, Gröhn OH, et al. B0 dependence of the on‐resonance longitudinal relaxation time in the rotating frame (T1ρ) in protein phantoms and rat brain in vivo. *Magn Reson Med*. 2004;51(1):4-8.
60. Pang Y, Palmieri‐Smith RM, Maerz T. An efficient R1 ρ dispersion imaging method for human knee cartilage using constant magnetization prepared turbo‐FLASH. *NMR Biomed*. 2021;34(6):e4500.
61. Lebel C, Gee M, Camicioli R, Wieler M, Martin W, Beaulieu C. Diffusion tensor imaging of white matter tract evolution over the lifespan. *Neuroimage*. 2012;60(1):340-352.
62. Bartels L, Doucette J, Birkl C, Zhang Y, Weber AM, Rauscher A. Orientation dependence of T2 in newborn white matter shows dipole-dipole interaction effects. In: Proceedings of the International Society of Magnetic Resonance Medicine, Virtual, 2021:2254.
63. Ohvo-Rekilä H, Ramstedt B, Leppimäki P, Slotte JP. Cholesterol interactions with phospholipids in membranes. *Progress in lipid research*. 2002;41(1):66-97.
64. Knight MJ, Smith‐Collins A, Newell S, Denbow M, Kauppinen RA. Cerebral white matter maturation patterns in preterm infants: an MRI T2 relaxation anisotropy and diffusion tensor imaging study. *Journal of Neuroimaging*. 2018;28(1):86-94.
65. Bloom M, Sternin E. Transverse nuclear spin relaxation in phospholipid bilayer membranes. *Biochemistry*. 1987;26(8):2101-2105.
66. Veraart J, Nunes D, Rudrapatna U, et al. Noninvasive quantification of axon radii using diffusion MRI. *Elife*. 2020;9:e49855.
67. Borthakur A, Wheaton AJ, Gougoutas AJ, et al. In vivo measurement of T1ρ dispersion in the human brain at 1.5 tesla. *J Magn Reson Imaging*. 2004;19(4):403-409.
68. Momot KI, Pope JM, Wellard RM. Anisotropy of spin relaxation of water protons in cartilage and tendon. *NMR Biomed*. 2010;23(3):313-24.
69. Mitsumori F, Watanabe H, Takaya N, et al. Toward understanding transverse relaxation in human brain through its field dependence. *Magnet Reson Med*. 2012;68(3):947-953.
70. Möller HE, Bossoni L, Connor JR, et al. Iron, myelin, and the brain: neuroimaging meets neurobiology. *Trends in neurosciences*. 2019;42(6):384-401.
71. Gent M, Prestegard J. Nuclear magnetic relaxation and molecular motion in phospholipid bilayer membranes. *J Magn Reson*. 1977;25(2):243-262.
72. Morrison C, Mark Henkelman R. A model for magnetization transfer in tissues. *Magnet Reson Med*. 1995;33(4):475-482.

EIGHT FIGURES

bioRxiv preprint doi: https://doi.org/10.1101/2021.09.13.460097; this version posted April 19, 2022. The copyright holder for this preprint (which was not certified by peer review) is the author/funder. All rights reserved. No reuse allowed without permission.

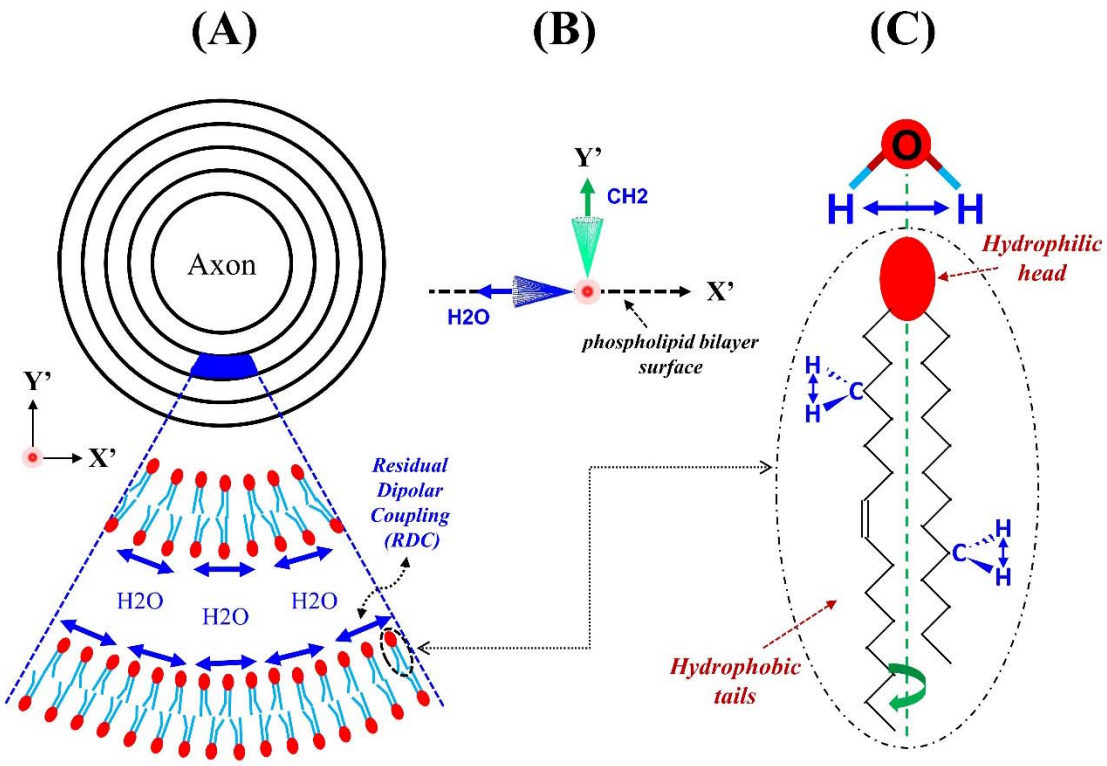

FIGURE 1 Schematics of residual dipolar coupling (RDC, blue double-headed arrows) organized around an axon fiber (A). A lipid molecule is highlighted (C) with RDCs (B) of ordered water and methylene (CH2) protons respectively perpendicular to and parallel to bilayer surface normal (green dashed line). Figures 1A and 1C were adapted from Figure 2 in the reference.[23]

bioRxiv preprint doi: https://doi.org/10.1101/2021.09.13.460097; this version posted April 19, 2022. The copyright holder for this preprint (which was not certified by peer review) is the author/funder. All rights reserved. No reuse allowed without permission.

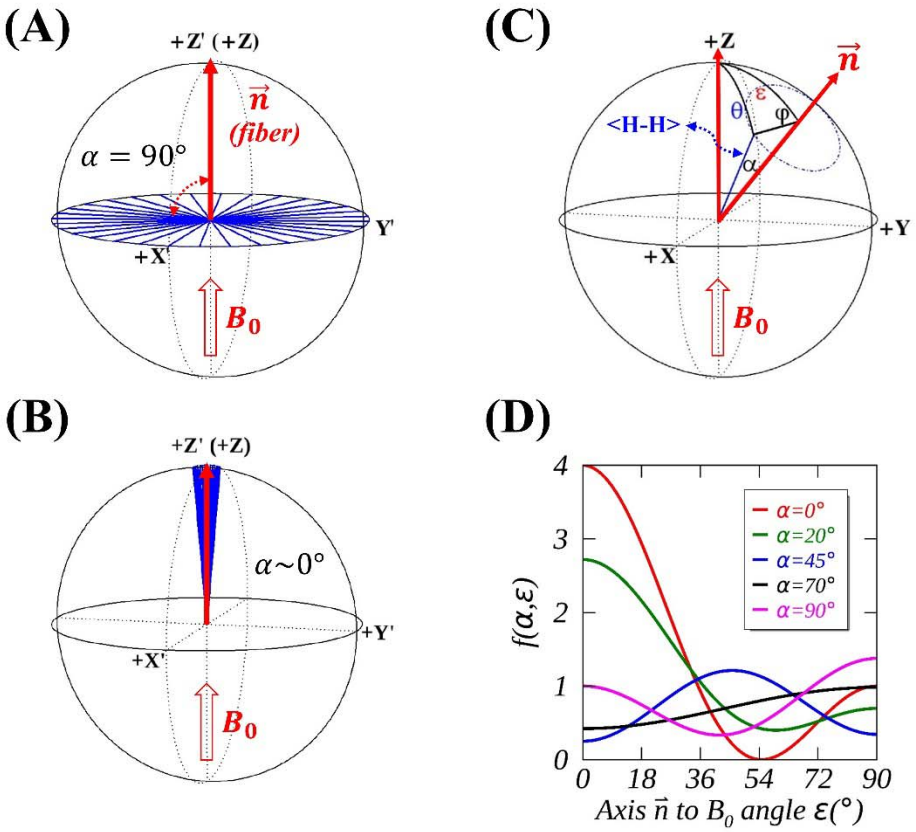

FIGURE 2 An axially symmetric model with an open angle α=90° (A) or $\alpha \sim 0°$ (B) when ε=0°, i.e., the primary axis ($\vec{n}$) of an axon fiber aligned with B_0. A general case with $\alpha \neq 0°$ and $\varepsilon \neq 0°$ is also presented (C) and five anisotropic R_2 orientation dependence $f(\alpha, \varepsilon)$ profiles are plotted (D) with α ranging from 0° (red) to 90° (magenta).

bioRxiv preprint doi: https://doi.org/10.1101/2021.09.13.460097; this version posted April 19, 2022. The copyright holder for this preprint (which was not certified by peer review) is the author/funder. All rights reserved. No reuse allowed without permission.

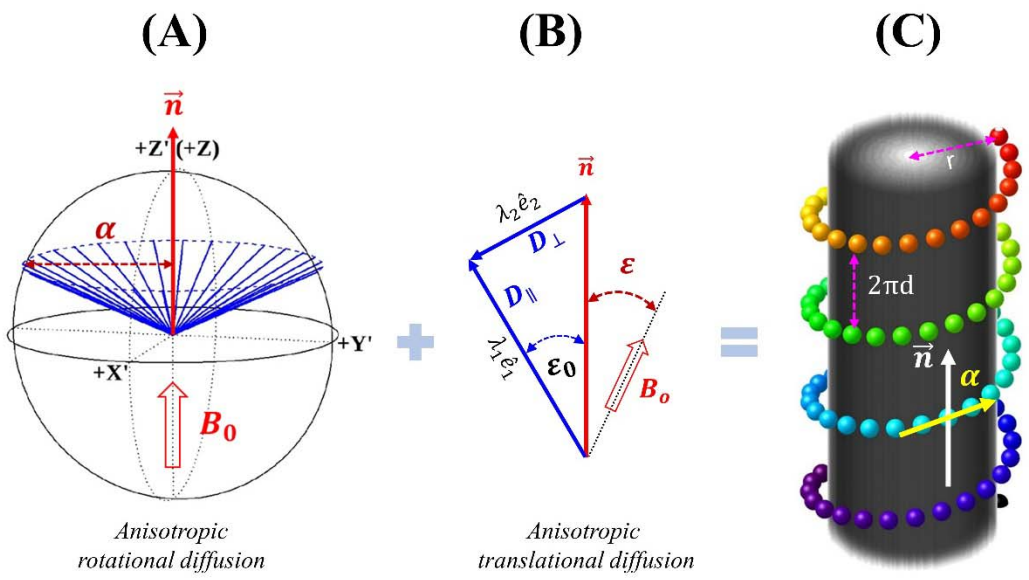

FIGURE 3 A combined anisotropic rotational diffusion (A) and anisotropic translational diffusion (B) into a cylindrical helix model (C), with an open angle α and circular helix parameters (i.e., r, radius and $2\pi d$, pitch) linked by $\tan\alpha = r/d$. An angle offset (ε_0) is determined by directional diffusivities ($D_{\parallel}$ and $D_{\perp}$).

bioRxiv preprint doi: https://doi.org/10.1101/2021.09.13.460097; this version posted April 19, 2022. The copyright holder for this preprint (which was not certified by peer review) is the author/funder. All rights reserved. No reuse allowed without permission.

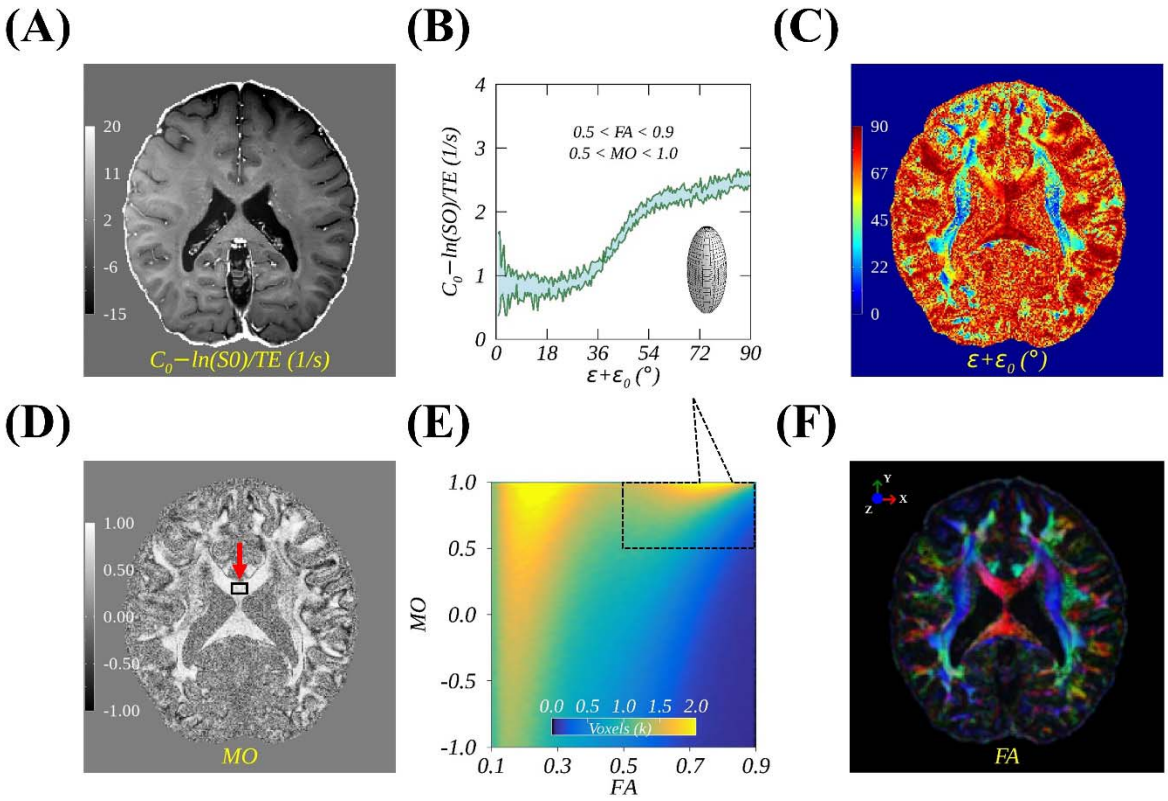

FIGURE 4 Average DTI parametric maps of anisotropic R_2=$C_0 - \ln(SO)/TE$ (A), directions of principal diffusivities (C), modes of anisotropies (D), and colored fractional anisotropies (F). An anisotropic R_2 orientation dependence profile (mean ± SD) (B) is shown for WM voxels defined (rectangular box) by limited FA and MO ranges (E) in whole brain. These DTI fits were derived from diffusion weighting data subsets (n=6) with b=0, 1000 s/mm^2, which are publicly available.[47]

bioRxiv preprint doi: https://doi.org/10.1101/2021.09.13.460097; this version posted April 19, 2022. The copyright holder for this preprint (which was not certified by peer review) is the author/funder. All rights reserved. No reuse allowed without permission.

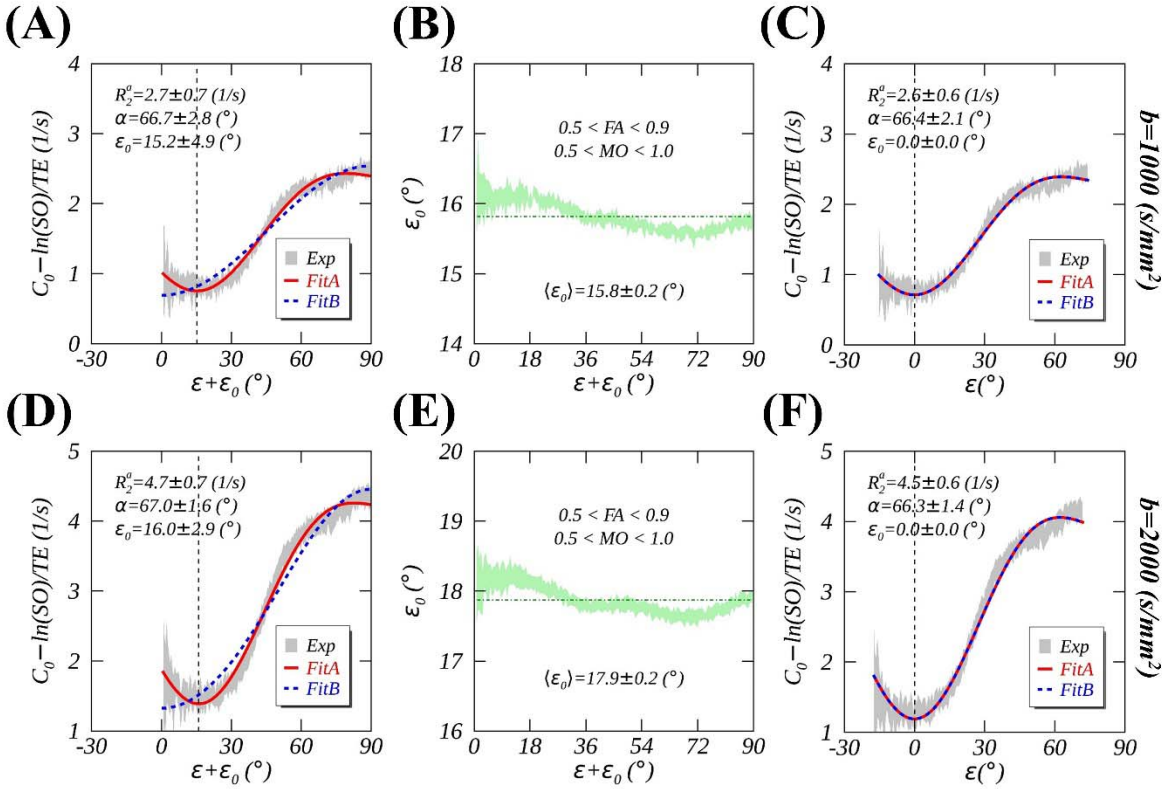

FIGURE 5 Demonstrations of angle offsets ε_0 depending on directional diffusivities. Anisotropic R_2 orientation dependences characterized by Fit A (red solid lines) and Fit B (blue dashed lines) before (A and D) and after (C and F) correcting angle offsets ε_0 for data with b=1000 s/mm^2 (A-C) and b=2000 s/mm^2 (D-F). Orientation dependences of ε_0 are also presented (B and E). These anisotropic R_2 profiles were generated from publicly available Connectome DTI datasets.[47]

bioRxiv preprint doi: https://doi.org/10.1101/2021.09.13.460097; this version posted April 19, 2022. The copyright holder for this preprint (which was not certified by peer review) is the author/funder. All rights reserved. No reuse allowed without permission.

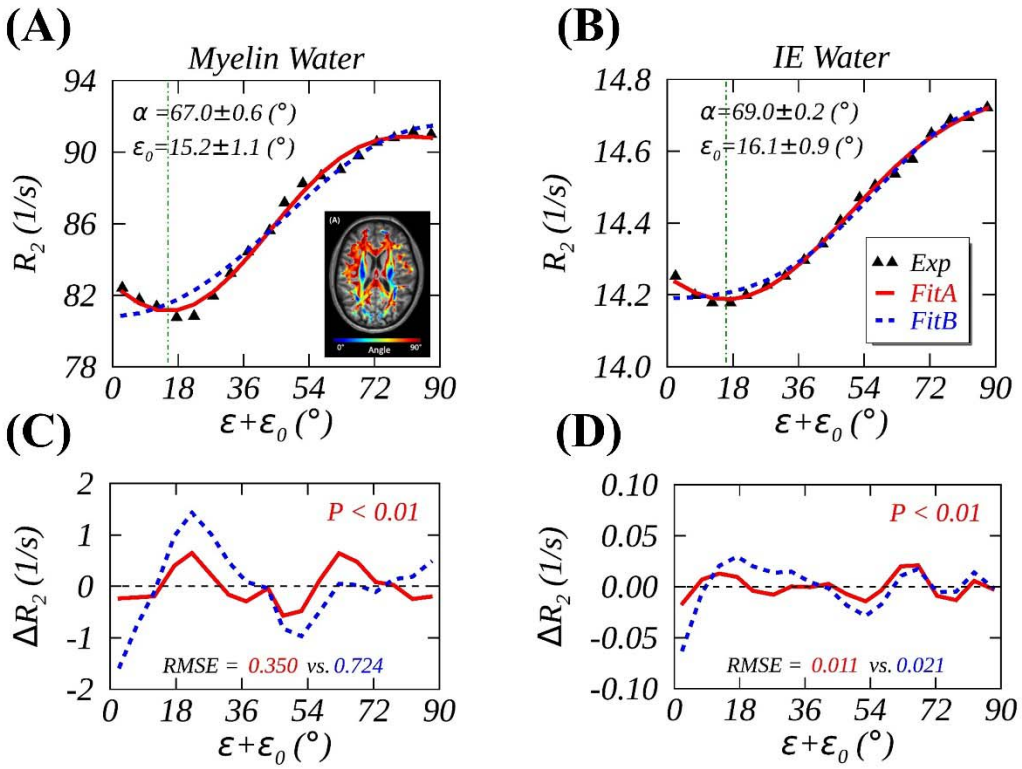

FIGURE 6 Measured (black triangles) and fitted (Fit A, red solid lines; Fit B, blue dashed lines) anisotropic R_2 of myelin water (A) and intra- and extracellular (IE) water (B) in human brain WM at 3T in vivo, with fitting residues ΔR_2=Fitted-Measured (C and D). The measured data and an inset image (A) were retrieved and adapted from the reference.[18]

bioRxiv preprint doi: https://doi.org/10.1101/2021.09.13.460097; this version posted April 19, 2022. The copyright holder for this preprint (which was not certified by peer review) is the author/funder. All rights reserved. No reuse allowed without permission.

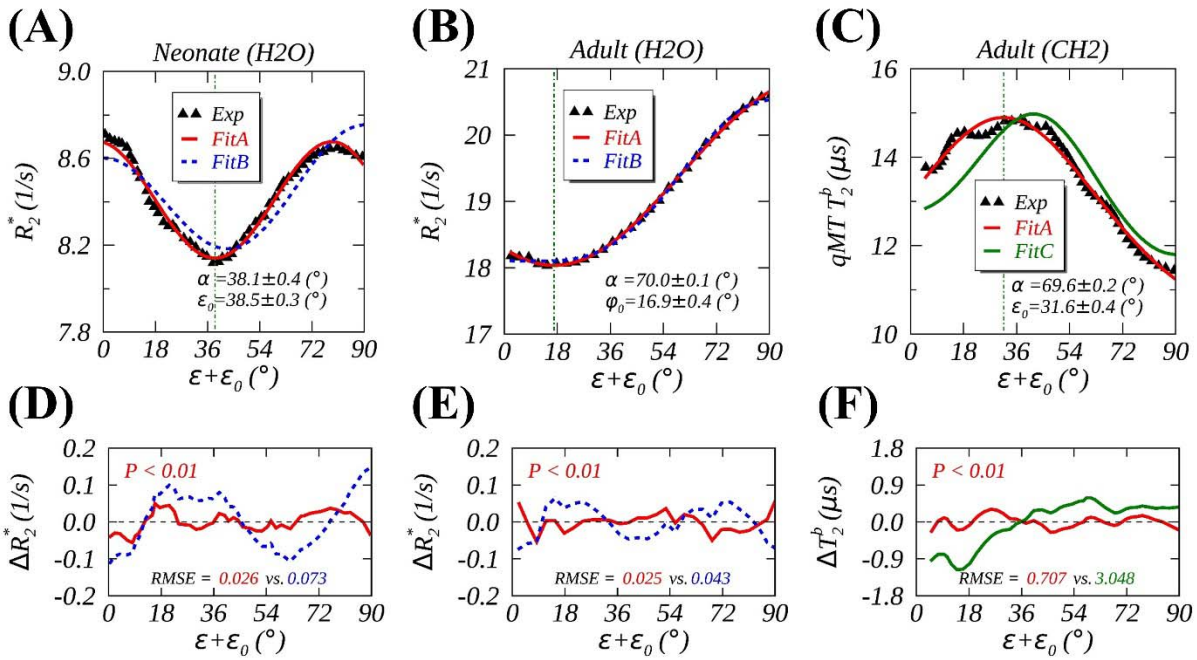

FIGURE 7 Measured (black triangles) and fitted (Fit A, red solid lines; Fit B, blue dashed lines, Fit C, green solid lines) anisotropic R_2^* from ordered water in WM of neonates (A), healthy adults (B), and T_2^b of semisolid macromolecules in WM of healthy adults (C) at 3T in vivo, with fitting residues ΔR_2=Fitted-Measured (D-F). The measured data were respectively retrieved from three references.[4, 17, 31]

bioRxiv preprint doi: https://doi.org/10.1101/2021.09.13.460097; this version posted April 19, 2022. The copyright holder for this preprint (which was not certified by peer review) is the author/funder. All rights reserved. No reuse allowed without permission.

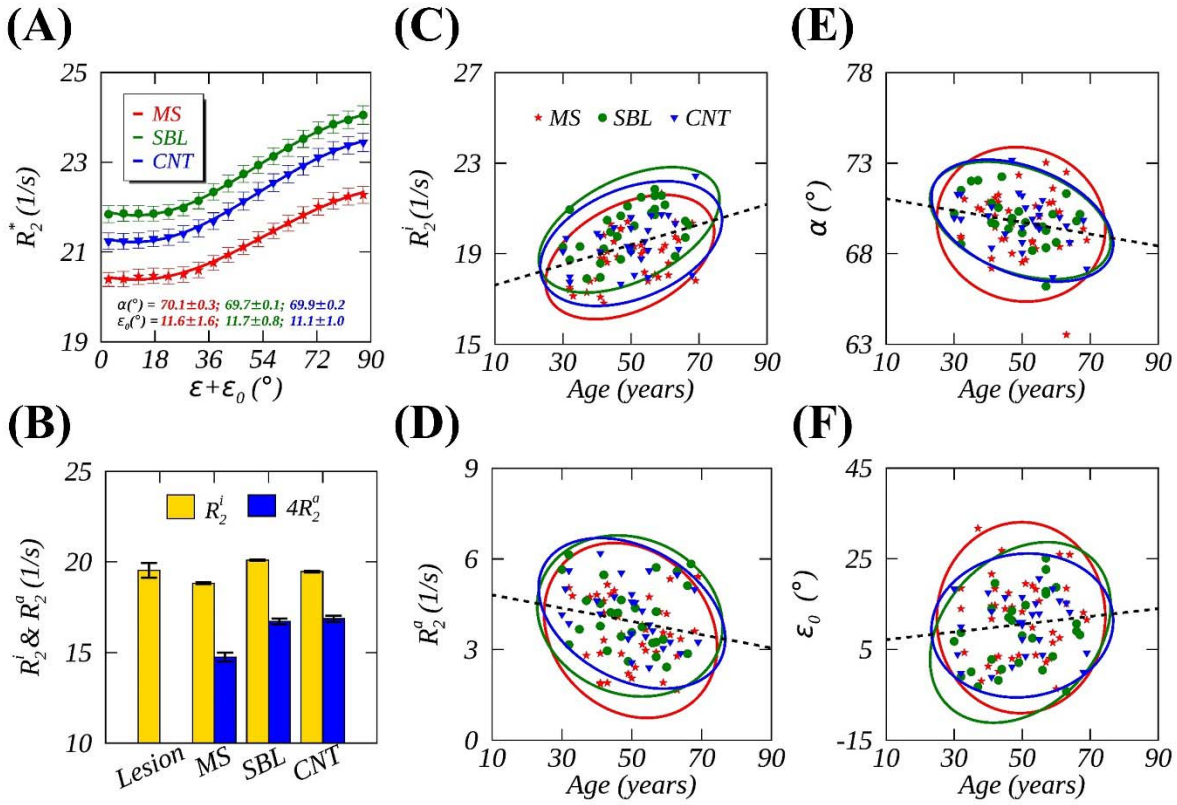

FIGURE 8 Measured (symbols) and fitted (Fit A, lines) anisotropic R_2^* in WM (A) from people with multiple sclerosis (MS, red) and two controls (SBL, green; CNT, blue), with the fitted α and ε_0 imprinted in colors, and with R_2^i and R_2^a represented by color bars including those from lesions (B). Correlations between the fits from individual subjects and their ages are displayed for R_2^i (C), R_2^a (D), α (E), and ε_0 (F), overlaid with 95% confidence ellipses from individual subgroups and linear regression lines (black dashed lines) from combined subgroups. The measured R_2^* data were retrieved from Supporting Information in the reference.[32]

bioRxiv preprint doi: https://doi.org/10.1101/2021.09.13.460097; this version posted April 19, 2022. The copyright holder for this preprint (which was not certified by peer review) is the author/funder. All rights reserved. No reuse allowed without permission.

SUPPORTING INFORMATION

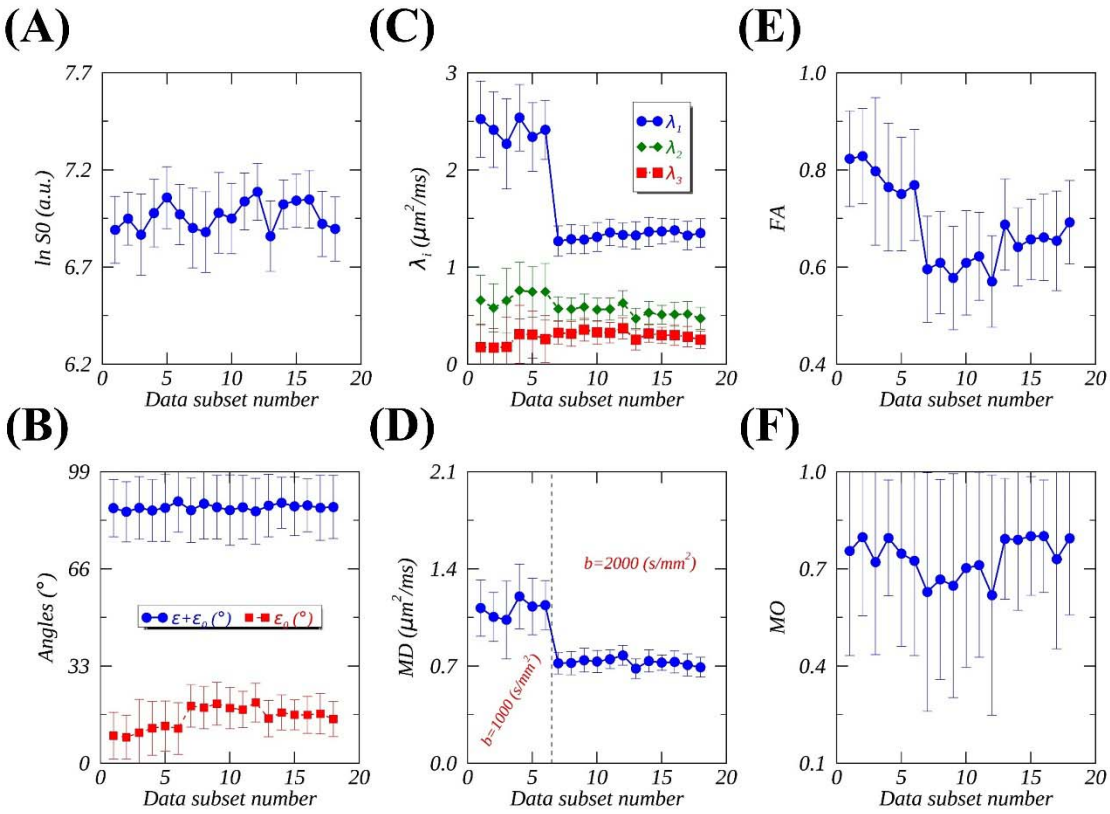

FIGURE S1 Examples of DTIFIT[48] output parameters averaged (mean ± SD) within a rectangular ROI from the corpus callosum (as highlighted in Fig. 4D) as well as angle offsets ε_0 (i.e., $\tan^{-1} D_\perp/D_\parallel$) for 18 diffusion weighting data subsets,[47] acquired using b-values (s/mm^2) of 1000 (n=1-6) and 2000 (n=7-18). Axial or principal ($D_\parallel$) and radial ($D_\perp$) diffusivities were defined as $D_\parallel = \lambda_1$ and $D_\perp = (\lambda_2+\lambda_3)/2$, assuming an axially symmetric diffusion tensor.

bioRxiv preprint doi: https://doi.org/10.1101/2021.09.13.460097; this version posted April 19, 2022. The copyright holder for this preprint (which was not certified by peer review) is the author/funder. All rights reserved. No reuse allowed without permission.

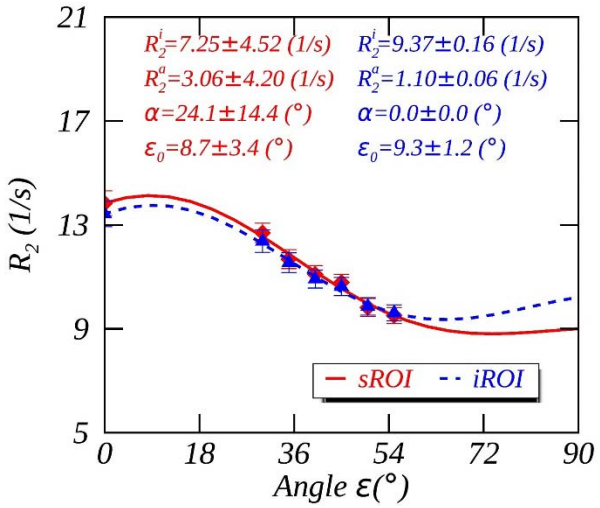

FIGURE S2 Magic angle effect in peripheral nervous system.[58] Anisotropic R_2 orientation dependences modeled using Fit A for two ROIs: (1) interfascicular space (sROI, red solid line) and (2) interfascicular space and intraneural nerve fascicles (iROI, blue dashed line).

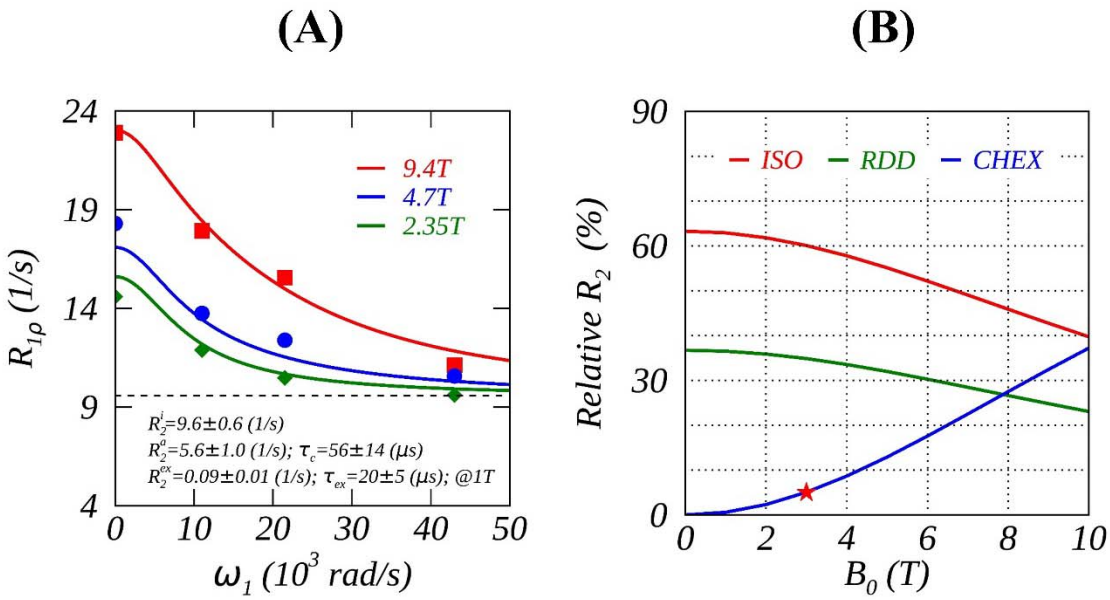

FIGURE S3 Separating B_0 dependent $R_{1\rho}$ dispersion[59] (A) into different contributions (B) on rat brain. $R_{1\rho}$ comprised a constant (ISO) and two dispersed components: (1) chemical exchange effect (CHEX) and (2) residual dipolar interactions (RDD) as demonstrated previously.[60] All orientation-independent and B_0-dependent relaxation mechanisms (including susceptibility

bioRxiv preprint doi: https://doi.org/10.1101/2021.09.13.460097; this version posted April 19, 2022. The copyright holder for this preprint (which was not certified by peer review) is the author/funder. All rights reserved. No reuse allowed without permission.

anisotropy) were lumped into CHEX that is proportional to B_0^2. When a spin-lock amplitude $\omega_1 = 0$, $R_{1\rho}$ became R_2 to which the relative CHEX contribution, i.e., 100*CHEX/(ISO+CHEX+RDD), was about 5% at 3T (red star, B).

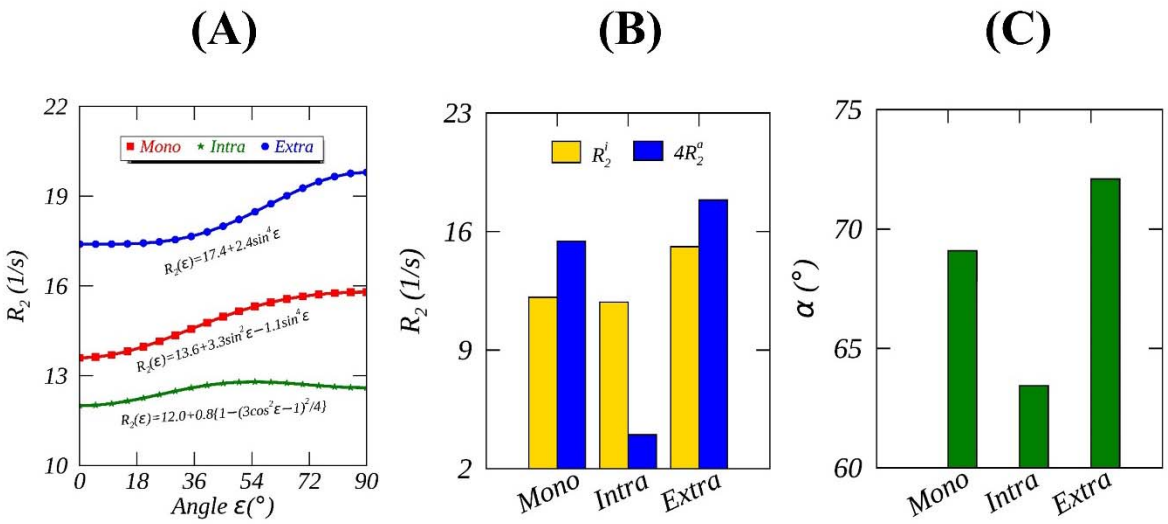

FIGURE S4 Recast best fitting functions (colored symbols, A) of mono-exponential (red), intra-(green) and extra-axonal (blue) transverse relaxation orientation dependences in WM into R_2^i and $4R_2^a$ (B), and an open angle α (C) using Fit A (colored solid lines, A). The original best fits were obtained from five healthy subjects, using a tiltable RF coil and diffusion-T_2 correlation MRI on a Connectome scanner.[7]

bioRxiv preprint doi: https://doi.org/10.1101/2021.09.13.460097; this version posted April 19, 2022. The copyright holder for this preprint (which was not certified by peer review) is the author/funder. All rights reserved. No reuse allowed without permission.

TWO TABLES

TABLE 1 The fits from Fit A (based on Eq. 4) for previously published anisotropic R_2 and R_2^* and related DTI metrics in WM in vivo at 3T. Data are denoted by means ± standard deviations or range (square brackets) if applicable.

Group ID	Type	Data (n)	Age (yrs)	R_2^i (1/s)	R_2^a (1/s)	α (°)	ε_0 (°)	FA	b-value (s/mm^2)
A	DTI	Adult (1)	30.0	n/a	2.7±0.7	66.7±2.8	15.2±4.9	[0.5, 0.9]	1000
					4.7±0.7	67.0±1.6	16.0±2.9		2000
B	CPMG	Myelin (8)	26.0 [21-33]	76.5±0.6	16.0±0.8	67.0±0.6	15.2±1.1	0.60±0.12	700
		IE (8)		13.8±0.0	1.0±0.0	69.0±0.2	16.1±0.9		700
C	GRE	Neonates (8)	0.78±0.02	7.2±0.1	1.3±0.1	38.1±0.4	38.5±0.3	0.31±0.01	700
D	GRE	Adults (16)	43.5±12.0	15.9±0.1	5.1±0.1	70.0±0.1	16.9±0.4	[0.4, 1.0]	1000
E	qMT	Adults (7)	26.0 [19-33]	46.9±1.3 (10^3)	50.0±2.3 (10^3)	69.6±0.2	31.6±0.4	[0.7, 1.0]	1000
F	GRE	MS (39)	49.7±10.1	18.9±1.1	3.6±1.2	69.6±1.7	12.0±8.6	n/a	1000
		SBL (28)	49.5±10.5	20.1±1.1	4.1±1.1	69.9±1.3	8.8±8.1	n/a	1000
		CNT (27)	50.0±10.7	19.5±1.1	4.2±1.0	69.8±1.4	10.3±6.5	n/a	1000

TABLE 2 Pearson correlation coefficients (PCC) between the fits (Fit A based on Eq. 4) of anisotropic R_2^* in WM and the ages of people from individual or combined subgroups (Group F). MS, multiple sclerosis; SBL, age-matched asymptomatic siblings; CNT, age-matched unrelated healthy subjects.

Fits	MS		SBL		CNT		ALL	
	PCC	*P*-value	PCC	*P*-value	PCC	P-value	PCC	*P*-value
$\boldsymbol{R_2^i}$	0.41	0.01	0.48	0.01	0.38	0.05	0.38	<0.01
$\boldsymbol{R_2^a}$	-0.19	0.25	-0.13	0.51	-0.34	0.08	-0.20	0.05
$\boldsymbol{\alpha}$	-0.06	0.72	-0.37	0.05	-0.38	0.05	-0.23	0.03
$\boldsymbol{\varepsilon_0}$	0.01	0.96	0.30	0.12	0.07	0.75	0.11	0.28

bioRxiv preprint doi: https://doi.org/10.1101/2021.09.13.460097; this version posted April 19, 2022. The copyright holder for this preprint (which was not certified by peer review) is the author/funder. All rights reserved. No reuse allowed without permission.

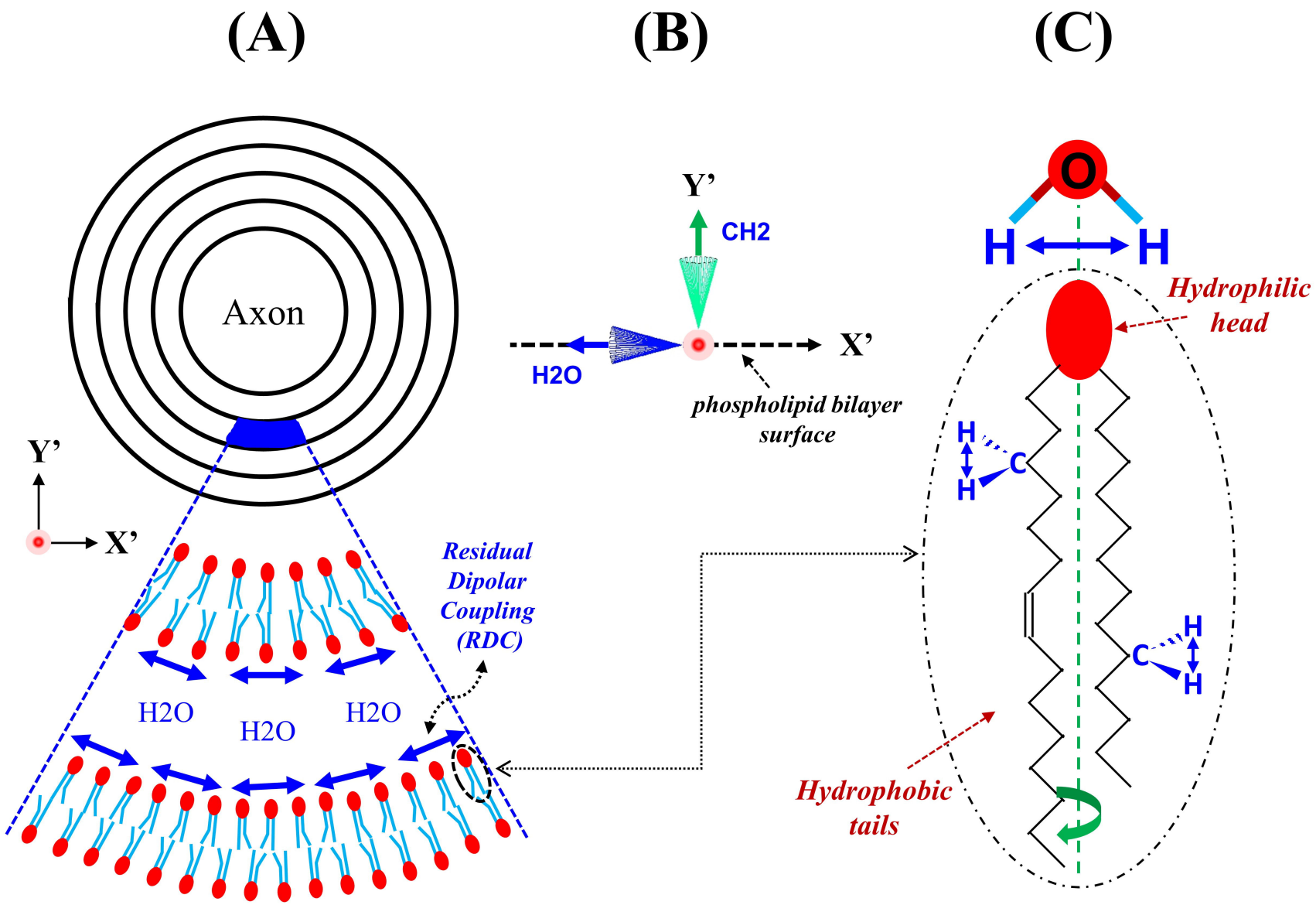
(A)
(B)
(C)
Axon
Y'
X'
H2O
H2O
H2O
Residual Dipolar Coupling (RDC)
Y'
CH2
X'
H2O
phospholipid bilayer surface
O
H
H
Hydrophilic head
H
C
H
C
H
H
Hydrophobic tails

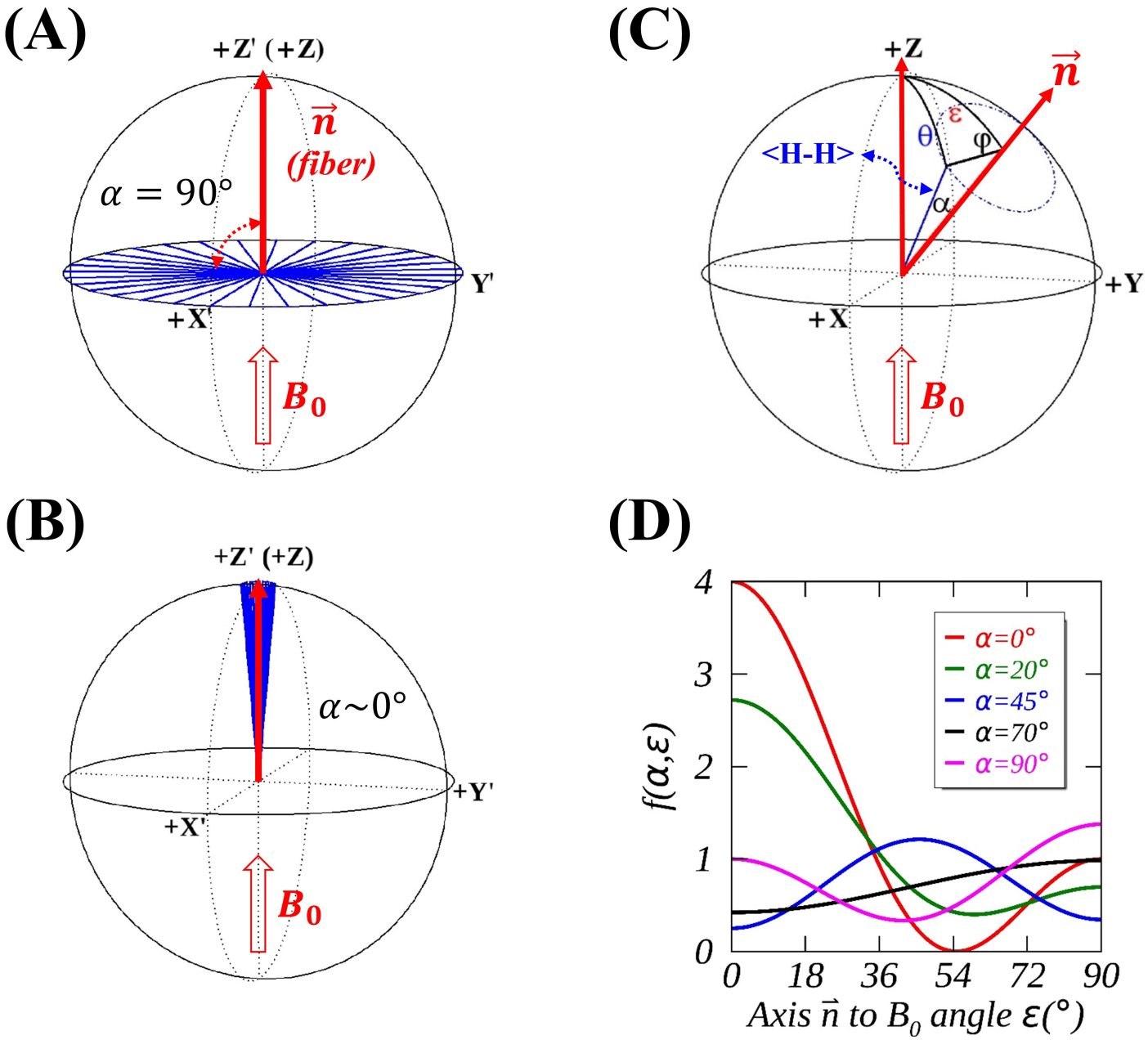
(A)
+Z' (+Z)
$\vec{n}$
(fiber)
α = 90°
Y'
+X'
B_0
(C)
+Z
$\vec{n}$
ε
θ
φ
<H-H>
α
+Y
+X
B_0
(B)
+Z' (+Z)
α~0°
+Y'
+X'
B_0
(D)
4
3
2
1
0
f(α,ε)
α=0°
α=20°
α=45°
α=70°
α=90°
0
18
36
54
72
90
Axis $\vec{n}$ to B_0 angle ε(°)

(A)

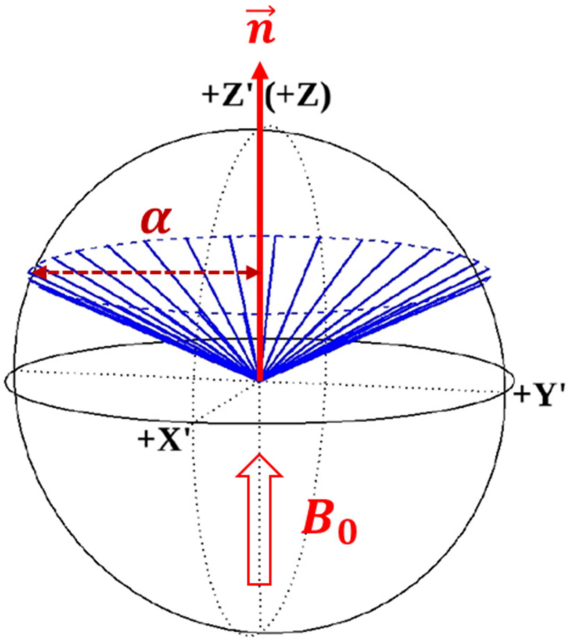

Anisotropic rotational diffusion

(B)

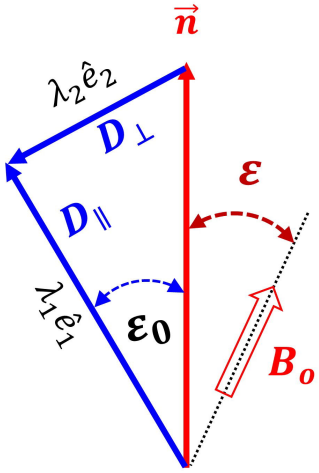

Anisotropic translational diffusion

(C)

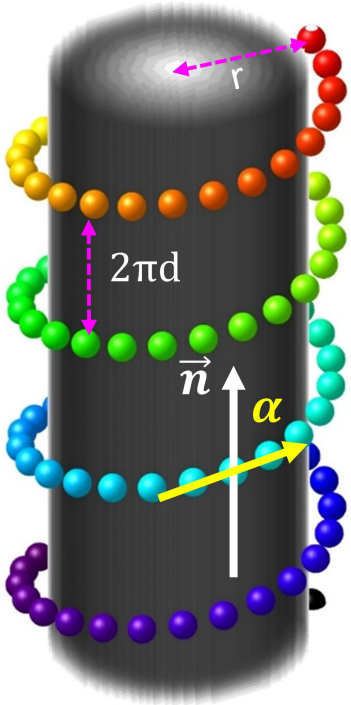

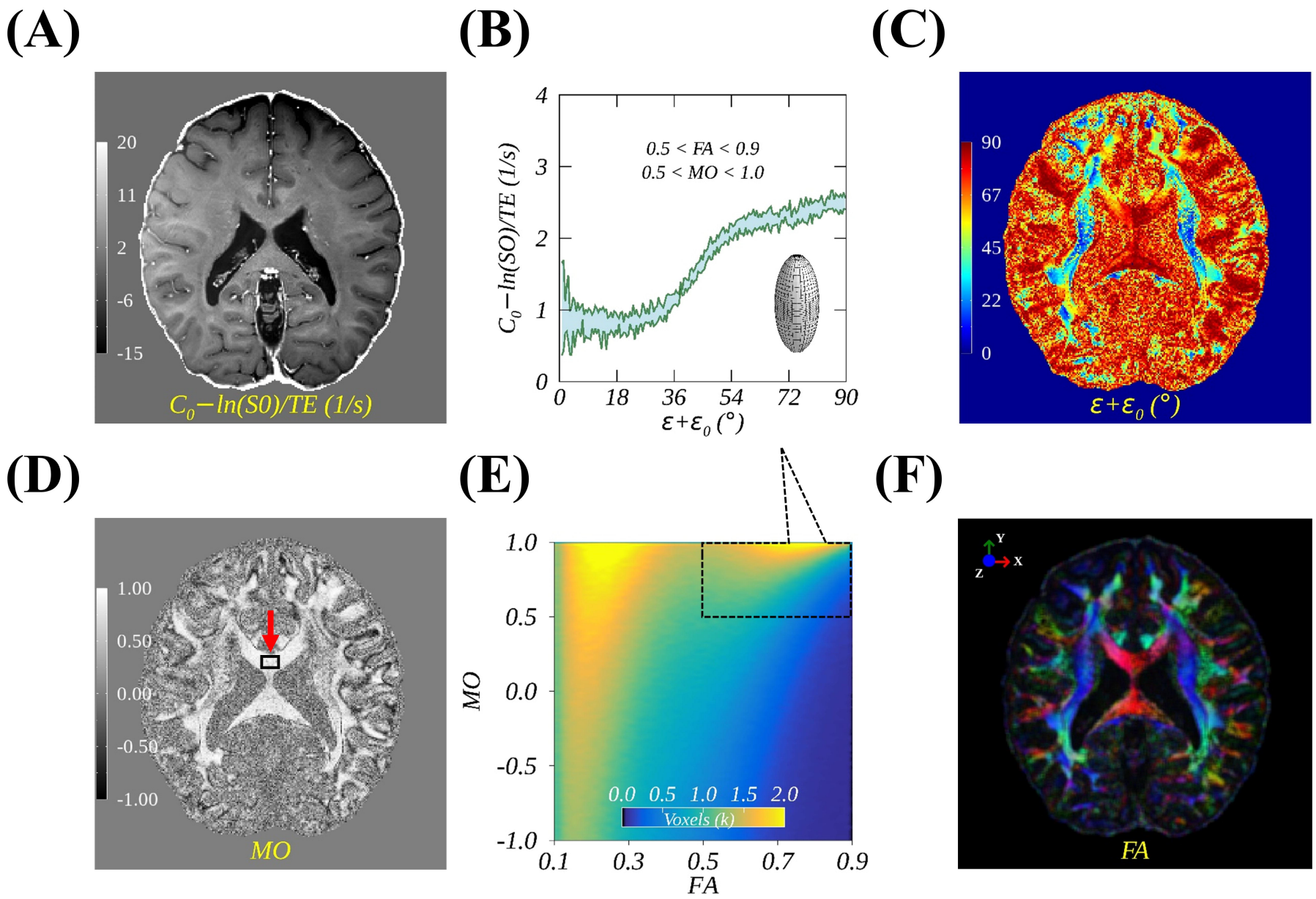
(A)
20
11
2
-6
-15
$C_0-ln(S0)/TE$ (1/s)
(B)
0.5 < FA < 0.9
0.5 < MO < 1.0
$C_0-ln(SO)/TE$ (1/s)
$\varepsilon+\varepsilon_0$ (°)
(C)
90
67
45
22
0
$\varepsilon+\varepsilon_0$ (°)
(D)
1.00
0.50
0.00
-0.50
-1.00
MO
(E)
MO
FA
0.0 0.5 1.0 1.5 2.0
Voxels (k)
(F)
Y
X
Z
FA

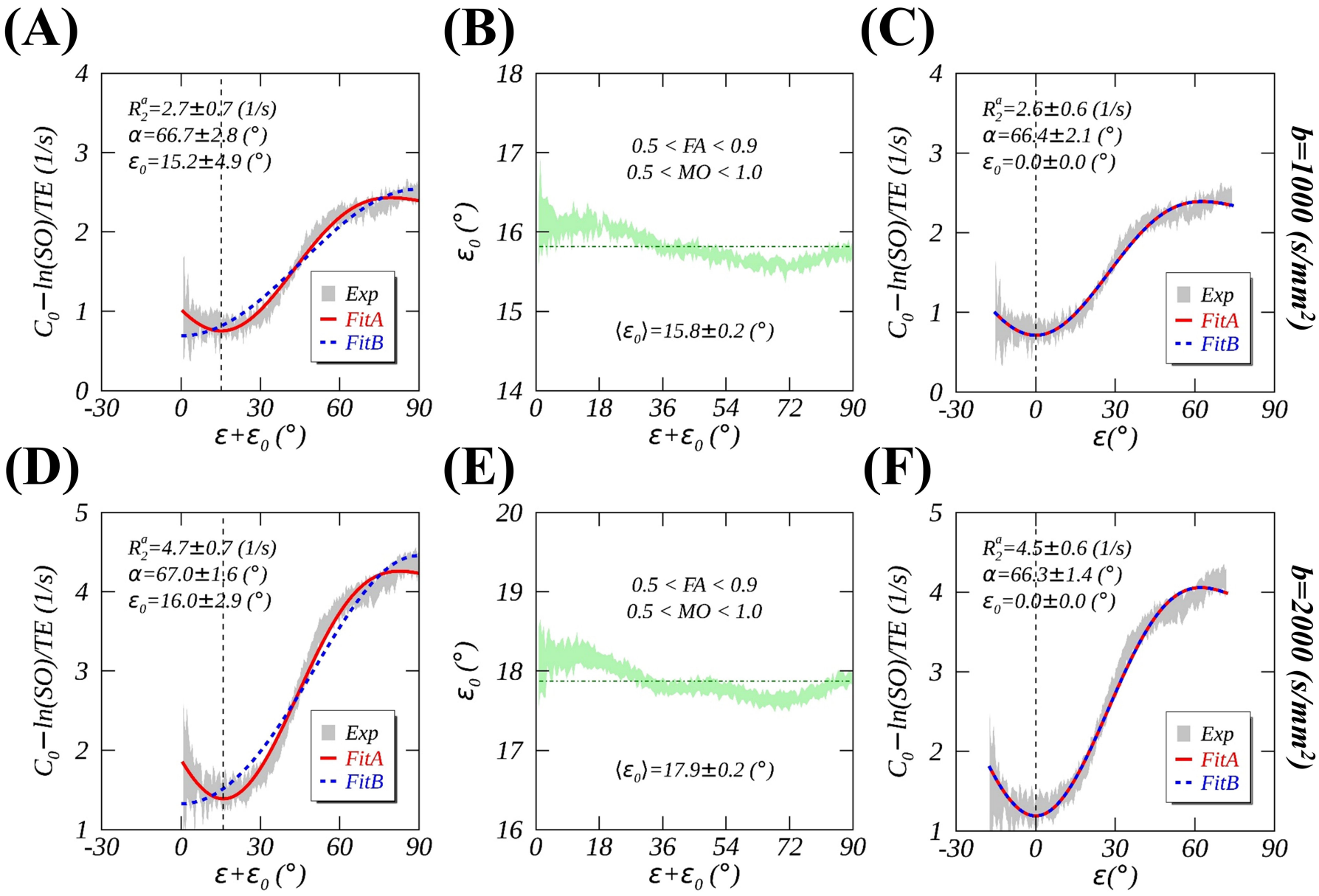
(A)
(B)
(C)
(D)
(E)
(F)
R_2^a=2.7±0.7 (1/s)
α=66.7±2.8 (°)
ε_0=15.2±4.9 (°)
0.5 < FA < 0.9
0.5 < MO < 1.0
⟨ε_0⟩=15.8±0.2 (°)
R_2^a=2.6±0.6 (1/s)
α=66.4±2.1 (°)
ε_0=0.0±0.0 (°)
b=1000 (s/mm²)
R_2^a=4.7±0.7 (1/s)
α=67.0±1.6 (°)
ε_0=16.0±2.9 (°)
⟨ε_0⟩=17.9±0.2 (°)
R_2^a=4.5±0.6 (1/s)
α=66.3±1.4 (°)
ε_0=0.0±0.0 (°)
b=2000 (s/mm²)
Exp
FitA
FitB
$C_0 - ln(SO)/TE$ (1/s)
ε_0 (°)
$\varepsilon+\varepsilon_0$ (°)
ε(°)

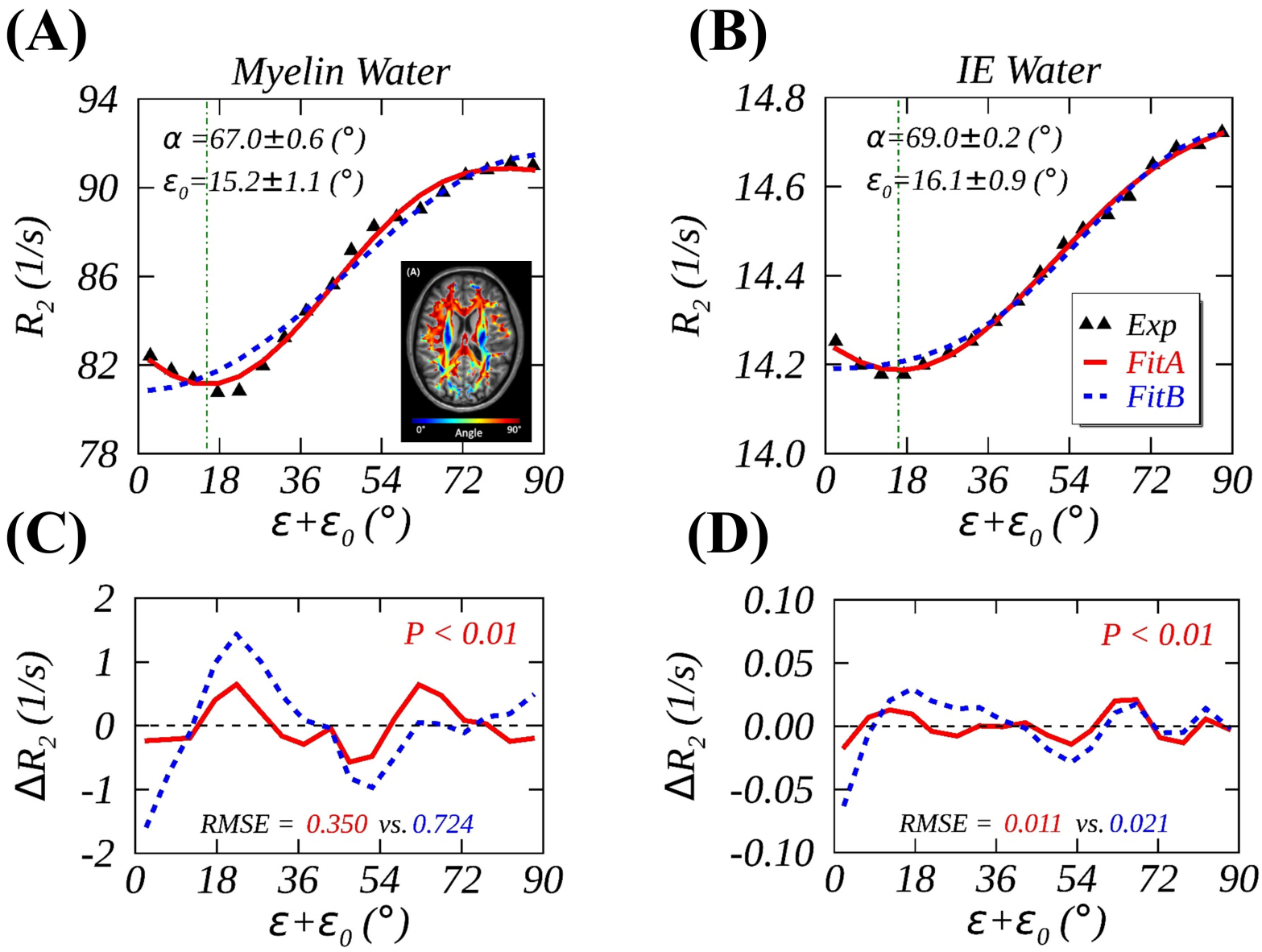
(A)
Myelin Water
α =67.0±0.6 (°)
ε0=15.2±1.1 (°)
R2 (1/s)
94
90
86
82
78
0
18
36
54
72
90
ε+ε0 (°)
(A)
0°
Angle
90°
(B)
IE Water
α=69.0±0.2 (°)
ε0=16.1±0.9 (°)
R2 (1/s)
14.8
14.6
14.4
14.2
14.0
Exp
FitA
FitB
ε+ε0 (°)
(C)
ΔR2 (1/s)
2
1
0
-1
-2
P < 0.01
RMSE = 0.350 vs. 0.724
ε+ε0 (°)
(D)
ΔR2 (1/s)
0.10
0.05
0.00
-0.05
-0.10
P < 0.01
RMSE = 0.011 vs. 0.021
ε+ε0 (°)

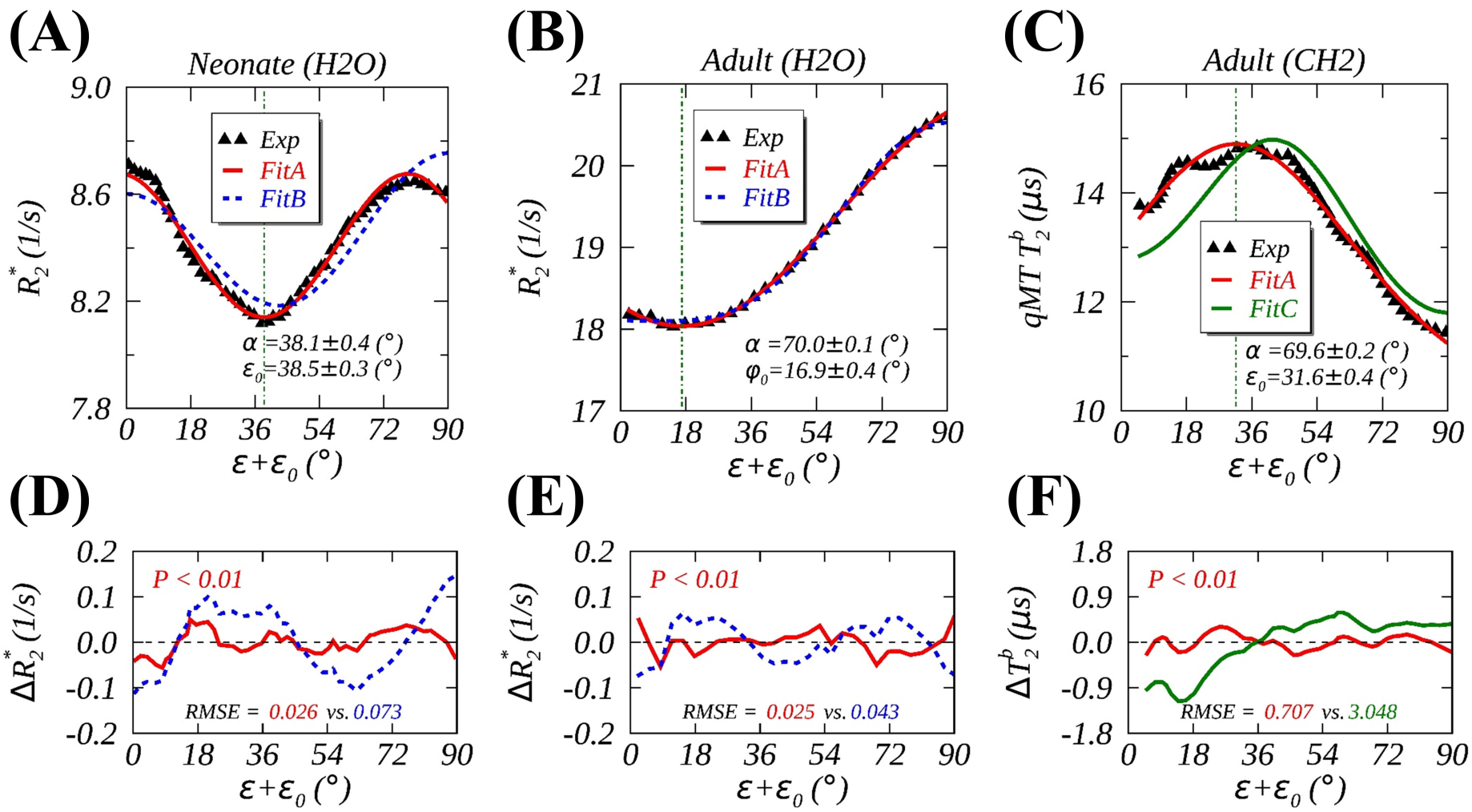
(A)
Neonate (H2O)
Exp
FitA
FitB
α =38.1±0.4 (°)
ε0=38.5±0.3 (°)
R2* (1/s)
ε+ε0 (°)
(B)
Adult (H2O)
Exp
FitA
FitB
α =70.0±0.1 (°)
φ0=16.9±0.4 (°)
R2* (1/s)
ε+ε0 (°)
(C)
Adult (CH2)
Exp
FitA
FitC
α =69.6±0.2 (°)
ε0=31.6±0.4 (°)
qMT T2b (μs)
ε+ε0 (°)
(D)
P < 0.01
RMSE = 0.026 vs. 0.073
ΔR2* (1/s)
ε+ε0 (°)
(E)
P < 0.01
RMSE = 0.025 vs. 0.043
ΔR2* (1/s)
ε+ε0 (°)
(F)
P < 0.01
RMSE = 0.707 vs. 3.048
ΔT2b (μs)
ε+ε0 (°)

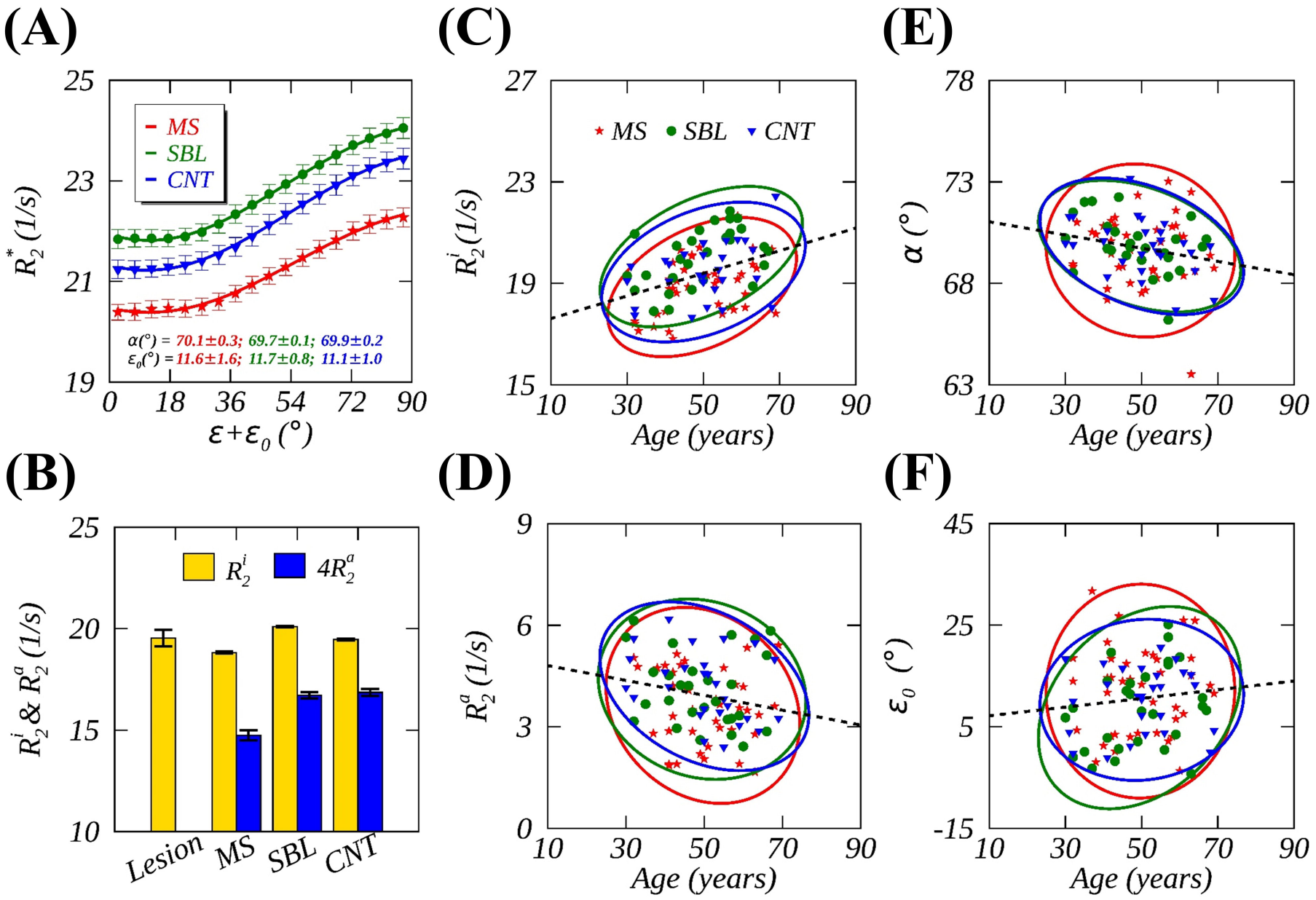
(A)
(B)
(C)
(D)
(E)
(F)
MS
SBL
CNT
R_2^* (1/s)
$\varepsilon+\varepsilon_0$ (°)
α(°) = 70.1±0.3; 69.7±0.1; 69.9±0.2
ε_0(°) = 11.6±1.6; 11.7±0.8; 11.1±1.0
R_2^i
$4R_2^a$
R_2^i & R_2^a (1/s)
Lesion
R_2^i (1/s)
Age (years)
R_2^a (1/s)
α (°)
ε_0 (°)

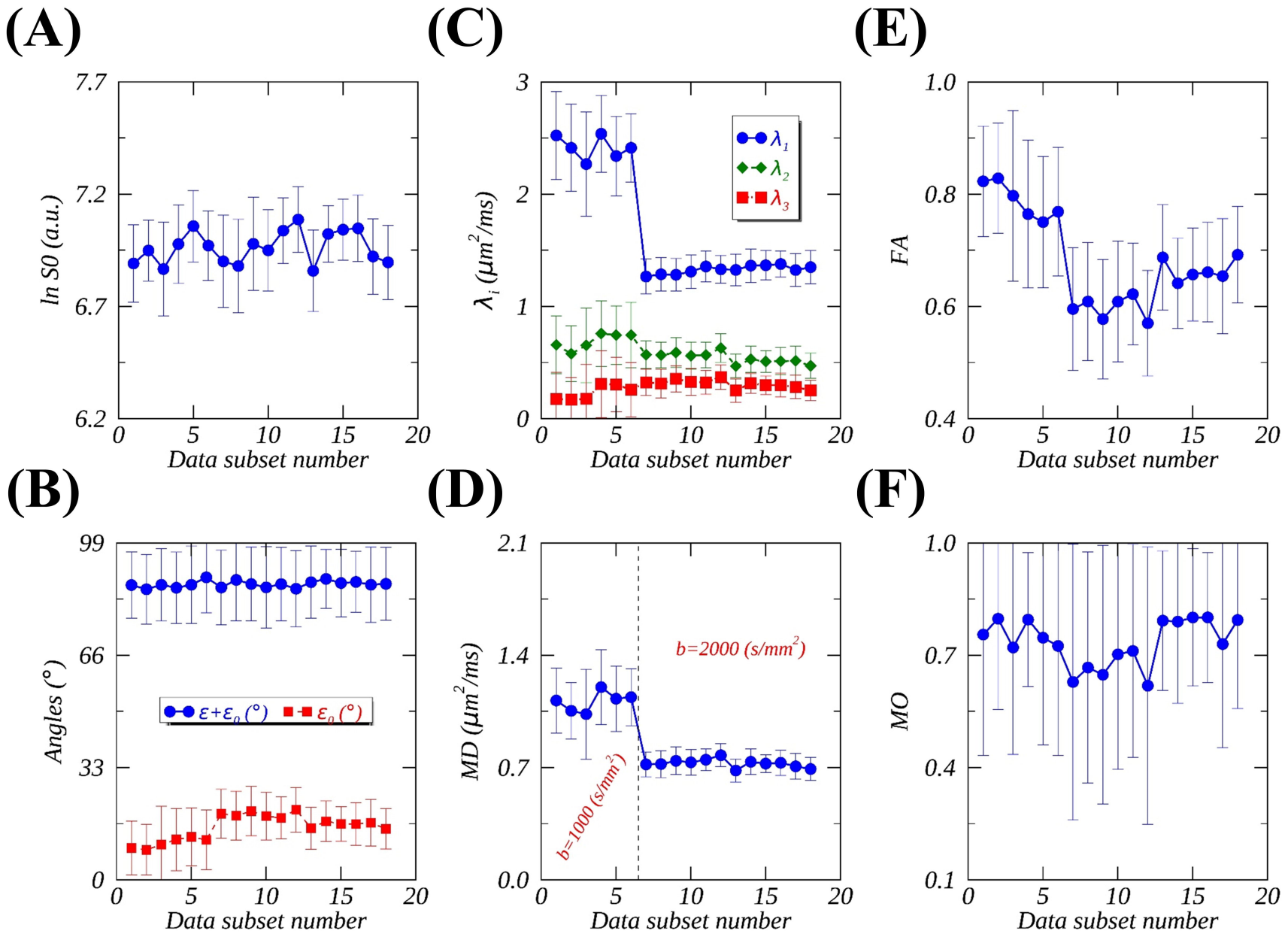
(A)
ln S0 (a.u.)
7.7
7.2
6.7
6.2
0
5
10
15
20
Data subset number
(C)
λ_i (μm^2/ms)
3
2
1
0
λ_1
λ_2
λ_3
Data subset number
(E)
FA
1.0
0.8
0.6
0.4
Data subset number
(B)
Angles (°)
99
66
33
0
$\varepsilon+\varepsilon_0$ (°)
ε_0 (°)
Data subset number
(D)
MD (μm^2/ms)
2.1
1.4
0.7
0.0
b=2000 (s/mm^2)
b=1000 (s/mm^2)
Data subset number
(F)
MO
1.0
0.7
0.4
0.1
Data subset number

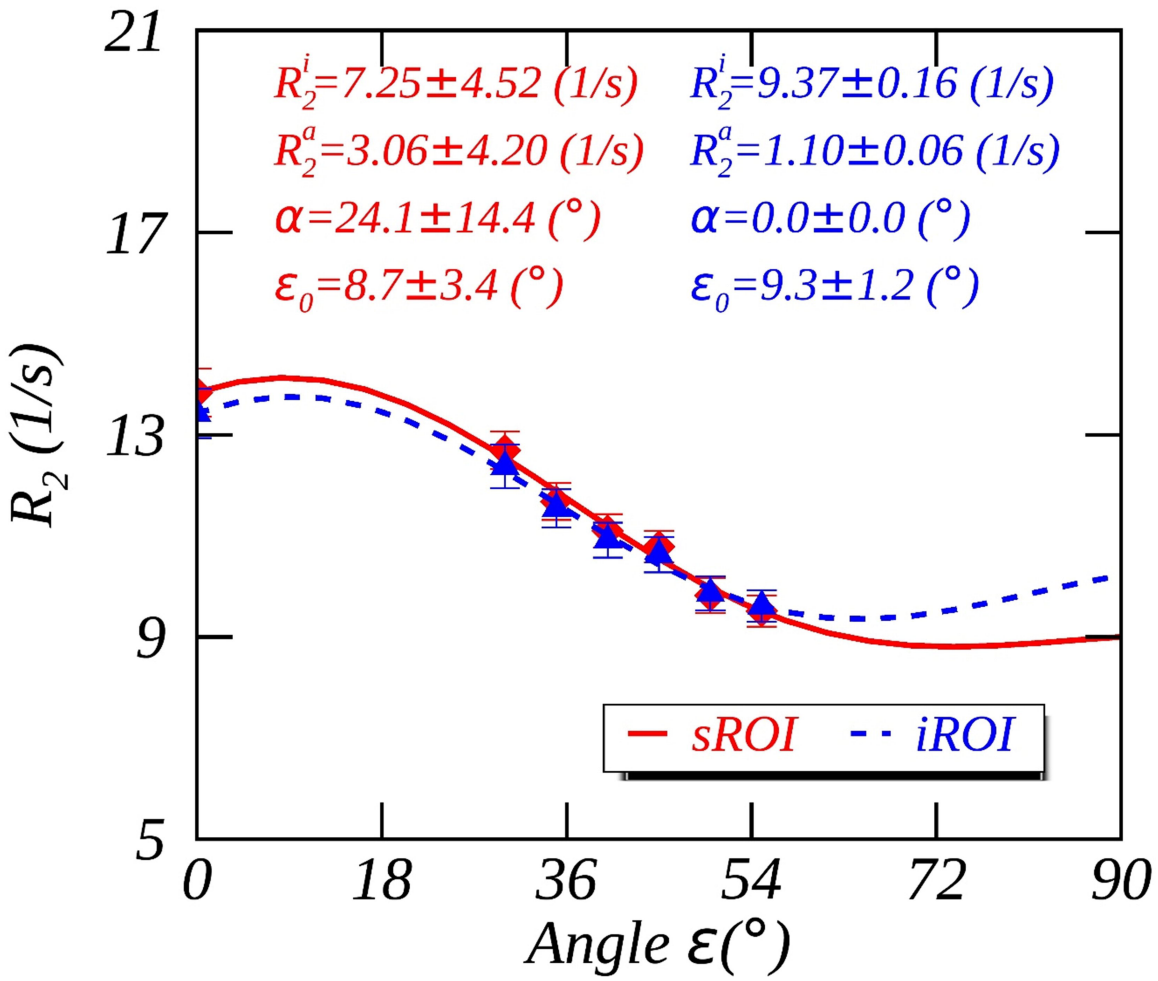
R_2^i=7.25±4.52 (1/s)
R_2^a=3.06±4.20 (1/s)
α=24.1±14.4 (°)
$ε_0$=8.7±3.4 (°)
R_2^i=9.37±0.16 (1/s)
R_2^a=1.10±0.06 (1/s)
α=0.0±0.0 (°)
$ε_0$=9.3±1.2 (°)
sROI
iROI
R_2 (1/s)
21
17
13
9
5
0
18
36
54
72
90
Angle ε(°)

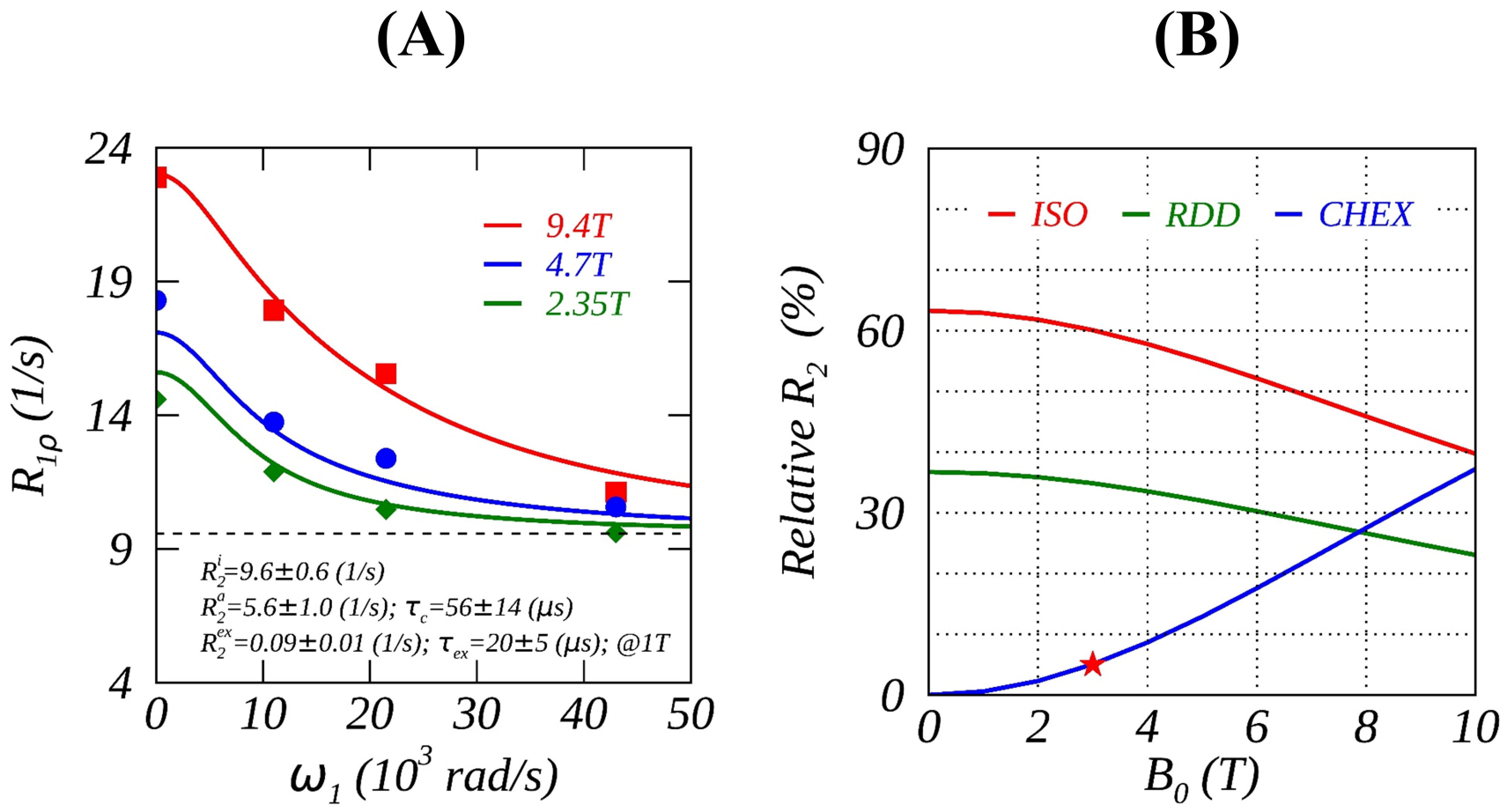
(A)
(B)
24
19
14
9
4
0
10
20
30
40
50
$R_{1\rho}$ (1/s)
ω_1 (10^3 rad/s)
9.4T
4.7T
2.35T
R_2^i=9.6±0.6 (1/s)
R_2^a=5.6±1.0 (1/s); τ_c=56±14 (μs)
R_2^{ex}=0.09±0.01 (1/s); τ_{ex}=20±5 (μs); @1T
90
60
30
0
2
4
6
8
10
Relative R_2 (%)
B_0 (T)
ISO
RDD
CHEX

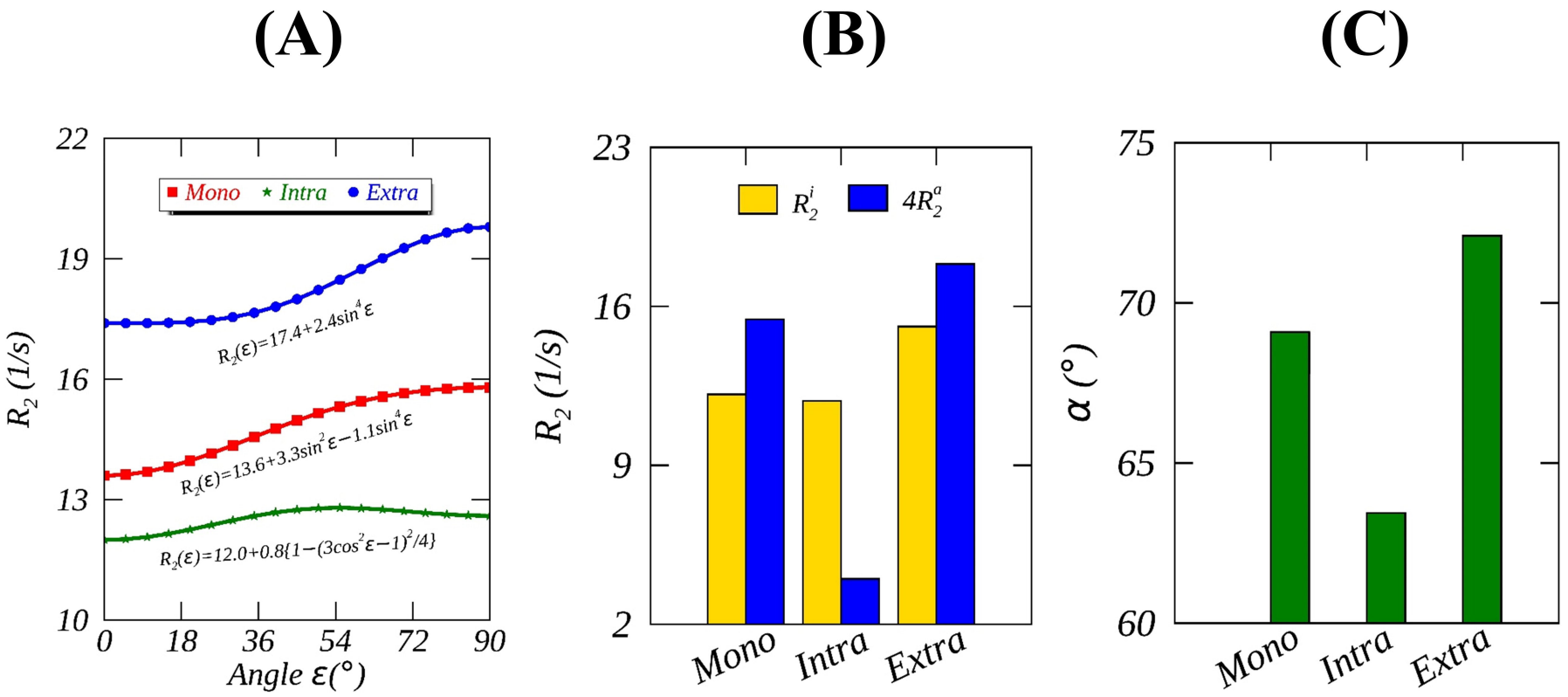
(A)
(B)
(C)
Mono
Intra
Extra
$R_2(\varepsilon)=17.4+2.4\sin^4\varepsilon$
$R_2(\varepsilon)=13.6+3.3\sin^2\varepsilon-1.1\sin^4\varepsilon$
$R_2(\varepsilon)=12.0+0.8\{1-(3\cos^2\varepsilon-1)^2/4\}$
R_2 (1/s)
Angle ε(°)
22
19
16
13
10
0
18
36
54
72
90
R_2^i
$4R_2^a$
23
16
9
2
α (°)
75
70
65
60

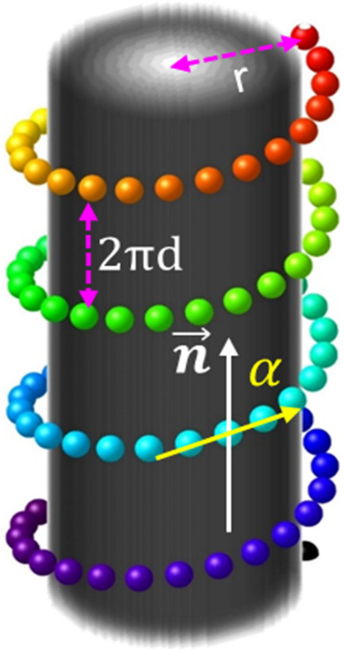
r
2πd
$\vec{n}$
α

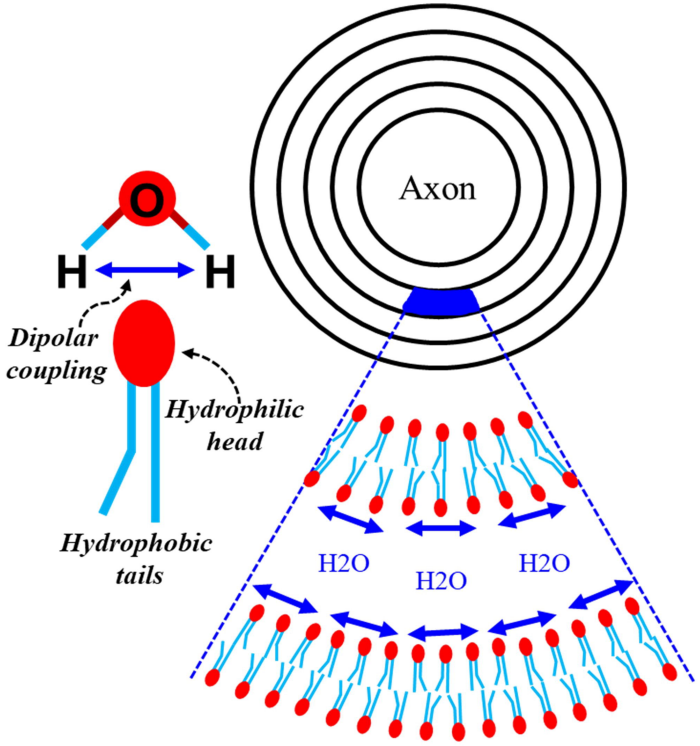
Axon
O
H
H
Dipolar coupling
Hydrophilic head
Hydrophobic tails
H2O
H2O
H2O

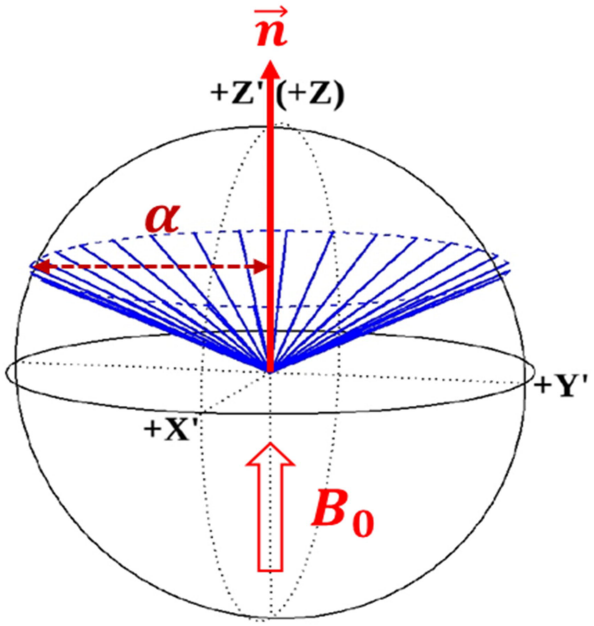
$\vec{n}$
+Z' (+Z)
α
+Y'
+X'
B_0

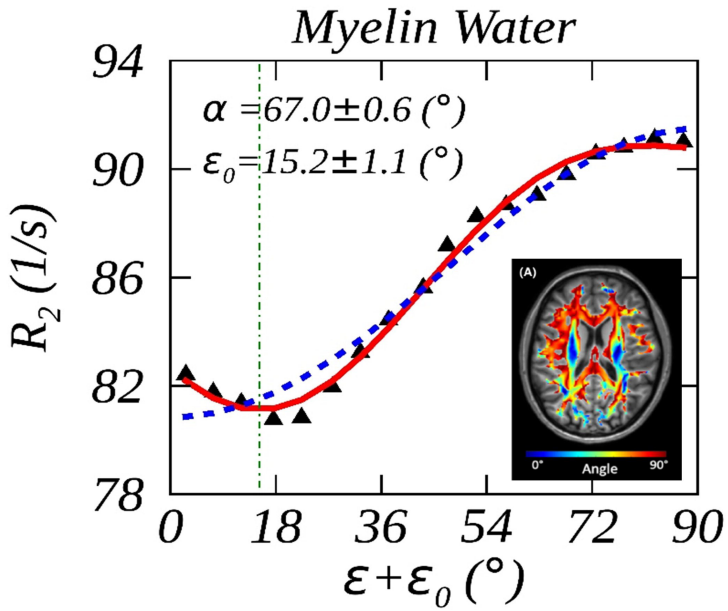
Myelin Water
α =67.0±0.6 (°)
ε_0=15.2±1.1 (°)
R_2 (1/s)
94
90
86
82
78
0
18
36
54
72
90
ε+ε_0 (°)
(A)
0°
Angle
90°